



RESEARCH ARTICLE

10.1029/2019JB017366

Key Points:

- Triaxial tests on gas reservoir sandstone show inelastic deformation (30%–50% of total) at all stages of compression
- At the small strains relevant to producing reservoirs (<1%), the inelastic part can be described by an isotropic plasticity model
- Modelling combined elastic plus inelastic deformation predicts more realistic reservoir stress changes than purely poroelastic estimates

Supporting Information:

- Supporting Information S1

Correspondence to:

R. P. J. Pijenburg,
r.p.j.pijenburg@uu.nl

Citation:

Pijenburg, R. P. J., Verberne, B. A., Hangx, S. J. T., & Spiers, C. J. (2019). Inelastic deformation of the Slochteren sandstone: Stress-strain relations and implications for induced seismicity in the Groningen gas field. *Journal of Geophysical Research: Solid Earth*, 124. <https://doi.org/10.1029/2019JB017366>

Received 16 JAN 2019

Accepted 22 APR 2019

Accepted article online 29 APR 2019

Inelastic Deformation of the Slochteren Sandstone: Stress-Strain Relations and Implications for Induced Seismicity in the Groningen Gas Field

R. P. J. Pijenburg¹ , B. A. Verberne^{1,2} , S. J. T. Hangx¹ , and C. J. Spiers¹

¹HPT Laboratory, Department of Earth Sciences, Utrecht University, Utrecht, Netherlands, ²Now at National Institute of Advanced Industrial Science and Technology, Geological Survey of Japan, Tsukuba, Japan

Abstract Pore pressure reduction in sandstone reservoirs generally leads to small elastic plus inelastic strains. These small strains (0.1%–1.0% in total) may lead to surface subsidence and induced seismicity. In current geomechanical models, the inelastic component is usually neglected, though its contribution to stress-strain behavior is poorly constrained. To help bridge this gap, we performed deviatoric and hydrostatic stress cycling experiments on Slochteren sandstone samples from the seismogenic Groningen gas field in the Netherlands. We explored in situ conditions of temperature ($T = 100$ °C) and pore fluid chemistry, porosities of 13% to 26% and effective confining pressures (≤ 320 MPa) and differential stresses (≤ 135 MPa) covering and exceeding those relevant to producing fields. We show that at all stages of deformation, including those relevant to producing reservoirs, 30%–50% of the total strain measured is inelastic. Microstructural observations suggest that inelastic deformation is largely accommodated by intergranular displacements at small strains of 0.5%–1.0%, with intragranular cracking becoming increasingly important toward higher strains. The small inelastic strains relevant for reservoir compaction can be described by an isotropic, Cam-clay plasticity model. Applying this model to the depleting Groningen gas field, we show that the in situ horizontal stress evolution is better represented by taking into account combined elastic and inelastic deformation than it is by representing the total deformation behavior using poroelasticity (up to 40% difference). Therefore, inclusion of the inelastic contribution to reservoir compaction has a key role to play in future geomechanical modelling of induced subsidence and seismicity.

1. Introduction

Pore pressure reduction accompanying the production of oil, gas, or geothermal fluids from sandstone reservoirs may lead to surface subsidence and induced seismicity (Evans et al., 2012; Fialko & Simons, 2000; Grünthal, 2014; Pratt & Johnson, 1926; van Wees et al., 2014). Both effects are caused by compaction of the reservoir, resulting from the increase in effective stress accompanying pore pressure reduction. Subsidence typically constitutes several tens of centimeters (Ketelaar, 2009; Mallman & Zoback, 2007; Morton et al., 2001), corresponding to vertical reservoir strains generally <1% (Cannon & Kole, 2017; Kole, 2015). The densely populated Groningen gas field located in the Netherlands (Figure 1) has attracted much attention in recent years, particularly since the occurrence of a damaging M_w 3.6 earthquake in 2012 (Dost & Kraaijpoel, 2013). In this field, the greatest subsidence (up to 34 cm, in 2013), the largest vertical strains (~0.3%; Cannon & Kole, 2017; Nederlandse Aardolie Maatschappij (NAM), 2015) and the largest and most frequently occurring seismic events (Figure 1a) are all seen in the central part of the field (Figure 1a), where the reservoir, the Slochteren sandstone, is thickest (~200 m) and most porous (18%–22%, Figure 1b).

Compaction of sandstone reservoirs may be in part elastic (reversible) and part inelastic (permanent). Quantifying the partitioning between elastic and inelastic contributions is essential for induced seismicity studies, as it directly affects in situ stress changes during pore pressure reduction (Chan et al., 2004; Pijenburg et al., 2018), as well as the elastic energy available to drive induced seismicity (Cooke & Madden, 2014; Pijenburg et al., 2018; Shipton et al., 2013). However, while the elastic component is well understood and easily quantified in terms of poroelasticity (Wang, 2000), the inelastic contribution has received little attention at reservoir-relevant strains (<1%). Rather, most previous research on sandstone mechanics (e.g., Baud et al., 2004; Rutter & Glover, 2012; Tembe et al., 2008; Wong et al., 1997) has focused on inelastic deformations developing at much larger compressive strains (2%–15%).

©2019. The Authors.

This is an open access article under the terms of the Creative Commons Attribution-NonCommercial-NoDerivs License, which permits use and distribution in any medium, provided the original work is properly cited, the use is non-commercial and no modifications or adaptations are made.

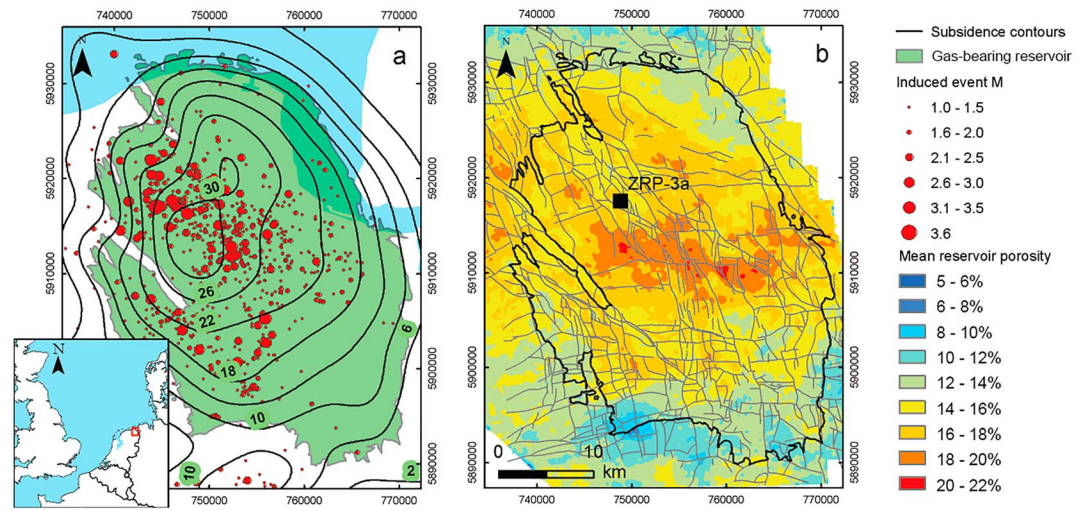


Figure 1. (a) Map showing the location of the Groningen gas field, the extent of the gas-bearing reservoir at approximately 3,000-m depth, contours of the surface subsidence measured in 2013, and induced earthquake magnitudes and locations in the period 1991–2017 (www.knmi.nl—seismic catalogue). (b) Map showing the mean (vertically averaged) porosity of the Slochteren reservoir sandstone (depth ~3,000 m) and the main faults (throw ranging up to 300 m; see Buijze et al., 2017) cutting the top of the reservoir. The porosity and subsidence data were provided courtesy of the field operator—see NAM (2013).

At the low temperature conditions ($T < 150\text{ }^{\circ}\text{C}$) and decade timescales relevant for fluid extraction from the upper crust ($< 5\text{ km}$), inelastic deformation of sandstone is believed to occur mostly through grain scale, brittle/frictional processes, including intergranular (grain boundary) cracking and slip (Bernabe et al., 1994; Menéndez et al., 1996; Pijenburg et al., 2018), as well as intragranular and transgranular cracking (Baud et al., 2004; Brantut et al., 2013; Heap et al., 2009, 2015). In addition, intergranular mass transfer (or pressure solution) may occur, although existing rate data (Chester et al., 2004; Niemeijer et al., 2002; Renard et al., 1999; Spiers et al., 2004; van Noort et al., 2008) suggest that the contribution of this slow creep process will be small. The extent to which each of these processes operates at a given temperature and timescale depends on the stresses imposed and on the stresses transmitted to the constituent grains, hence on the porosity (ϕ).

Experimental studies based on conventional deviatoric and hydrostatic testing (Wong & Baud, 2012, and references therein) generally express the mechanical behavior shown by sandstones in terms of mean effective stress ($P = [\sigma_1 + \sigma_2 + \sigma_3]/3$ —pore pressure P_p) versus total porosity reduction ($\Delta\phi_t$) data (Figure 2). Such $P - \Delta\phi_t$ curves typically show a transition from initial, nonlinear, concave-up behavior (Stage 1), followed by near-linear behavior (Stage 2), which in turn is followed by nonlinear behavior, characterized by dilation at low P and ϕ (Stage 3d—suffix d for dilation) and by nonlinear compaction at high P and ϕ (Stage 3—suffix c for compaction). The initial Stages 1 and 2 frequently show similar behaviors in deviatoric and hydrostatic compression (Baud et al., 2000; Wong et al., 1997), suggesting roughly isotropic behavior. During low P , deviatoric compression, deviation from the hydrostatic $P - \Delta\phi_t$ trend characterizes the onset of dilatancy (i.e., Stage 3d—see Figure 2) and is in this work marked by the mean effective stress P_{stage3d} . The mean effective stress marking the onset of nonlinear compaction (Stage 3c) is referred to as P_{stage3c} . Hence, in the present study, these terms are preferred over the

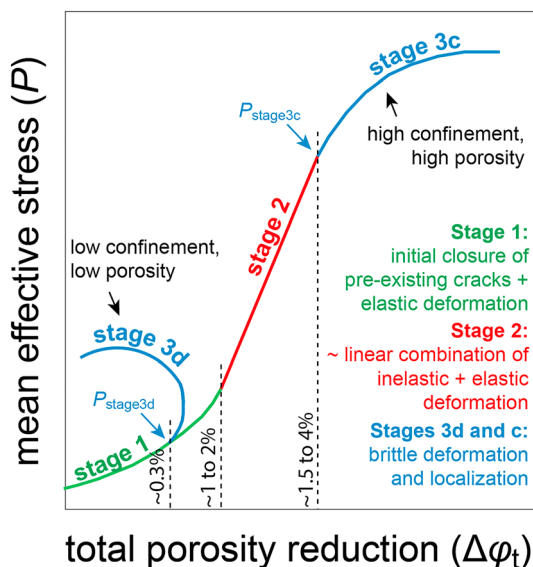


Figure 2. Schematic diagram showing the different stages in mean effective stress (P) versus total porosity reduction ($\Delta\phi_t$) behavior typically seen in mechanical testing of sandstones. (see in-text references). Note the effects of low porosity and confining pressure and low porosity and high confining pressure on Stage 3 behavior (dilation—suffix “d” versus compaction—“c”). The deformation mechanisms inferred in the literature are shown per stage, as are typical values of $\Delta\phi_t$ measured at the end of each stage.

more commonly used factors C' , C^* , and P^* , defined in the pioneering work by Zhang et al. (1990) and Wong et al. (1997). While it was recognized by these authors that inelastic deformation may occur at stresses below C' , C^* , and P^* (see also Menéndez et al., 1996), these thresholds are often effectively treated as elastic-inelastic yield points, with poroelasticity theory applying at lower stress levels (e.g., Brantut et al., 2014; Guéguen & Fortin, 2013; Wong et al., 1997; Wong & Baud, 2012). To avoid the connotation that the onset of dilation or nonlinearity corresponds to the onset of inelastic behavior, P_{stage3d} and P_{stage3c} are used instead.

The compliant, concave-up behavior seen in Stage 1 is thought to reflect poroelastic deformation, combined with semirecoverable closure of preexisting damage or cracks (David et al., 2012; Walsh, 1965). Stage 1 typically persists up to $\Delta\varphi_t$ values in the range of 0.3% (at low-effective confining pressures $P_c^{\text{eff}} = \text{confining pressure } P_c - P_p$ and at low φ) to 2.0% (high P_c^{eff} , high φ). The near-linear behavior seen in Stage 2 is in the bulk of the literature treated as if reflecting purely poroelastic deformation (Baud et al., 2000, 2004, 2006; Brantut et al., 2013; Klein et al., 2001; Heap et al., 2009, 2015; Rutter & Glover, 2012; Wong & Baud, 2012). However, the most recent experimental studies, including previous work on the Slochteren sandstone (Hol et al., 2015, 2018; Pijenburg et al., 2018), have shown that this near-linear behavior in fact reflects combined elastic and inelastic behavior, where the inelastic part constitutes some 20% to 70% of the total deformation (see also Bernabe et al., 1994). At $P_c^{\text{eff}} > 20$ MPa, Stage 2 behavior typically persists up to $\Delta\varphi_t$ values of 1.5%–4.0%, then giving way to Stage 3c (nonlinear compaction). At lower P_c^{eff} , Stage 1 transitions directly into Stage 3d at $\Delta\varphi_t \approx 0.3\%$. In both cases, Stages 3c and 3d are accompanied by pervasive intragranular cracking and intergranular or interparticle shear, frequently localizing in shear fractures (Stage 3d), or compaction bands (Stage 3c; Baud et al., 2004; Fortin et al., 2005; Tembe et al., 2008; Wu et al., 2000).

On the above basis, notably the latest experiments on Slochteren sandstone (Hol et al., 2015, 2018; Pijenburg et al., 2018) and earlier tests (Bernabe et al., 1994), it is increasingly clear that inelastic deformation contributes significantly to the compressive deformation of sandstone at the small strains (<1%) relevant for producing reservoirs. However, most geomechanical models addressing induced subsidence and seismicity ignore any inelastic contribution to the deformation of the reservoir and describe compaction using a simple compaction coefficient, in effect a poroelastic stiffness or compliance constant (Bourne et al., 2014; Dempsey & Suckale, 2017; Lele et al., 2016; Mulders, 2003; Postma & Jansen, 2018; van Eijs et al., 2006; Wassing et al., 2016; Zbinden et al., 2017). When an inelastic contribution is included, it is typically described using plasticity theory, originally developed to represent the inelastic deformation behavior of incohesive soils (Chan et al., 2004; Crawford et al., 2011; Crawford & Yale, 2002; Fredrich & Fossum, 2002; Han et al., 2005). Common examples of soil mechanics models utilizing plasticity theory include the critical state model (Schofield & Wroth, 1968), the cap model (DiMaggio & Sandler, 1971), and the modified Cam-clay model (Muir Wood, 1991). These models are characterized by a yield envelope which is elliptical in differential stress ($Q = \sigma_1 - \sigma_3$) versus mean effective stress (P) space. This yield envelope expands due to inelastic porosity reduction during compressive deformation, reflecting strain hardening due to densification. While strain hardening behavior has been observed in cohesive sandstones in qualitative terms (Rutter & Glover, 2012; Wong et al., 1992; Wong & Baud, 1999), at least the high strain, compactive Stage 3c behavior (see Figure 2) appears to be poorly described by plasticity theory (Baud et al., 2006). The extent to which plasticity models can describe Stages 1 and 2 behavior at the smaller strains relevant for depleting reservoirs remains unclear and insufficiently tested against experiments. Still, if applicable, plasticity models provide a convenient framework for quantifying the inelastic behavior of sandstone reservoir rocks not least because they are often already included in the finite element modelling packages used in geomechanics (e.g., Abaqus, Ansys, and DIANA).

In this paper, we investigate to what extent, if at all, the inelastic deformation behavior shown by the Slochteren sandstone from the Groningen gas field can be described by an isotropic plasticity model. To that end, we systematically quantify the elastic and inelastic deformation behavior characterizing all three stages of deformation commonly seen in sandstones (Figure 2), including the small strain behavior relevant for compacting reservoirs. This was done by performing both hydrostatic and deviatoric (differential) stress cycling experiments, under in situ conditions of temperature ($T = 100$ °C) and pore fluid chemistry, using samples with a range of porosities ($\varphi = 13\%$ to 26%) covering that observed in the field. Quantitative microstructural investigation of undeformed and deformed sample material was used to identify the

microphysical mechanisms accommodating inelastic deformation during Stages 1, 2, 3c, and 3d. In addition, an isotropic, Cam-clay-type plasticity model was fitted to the mechanical data to assess its applicability to describe and compute the inelastic response of the Slochteren sandstone to pore pressure reduction. Finally, we apply our results to assess the importance of including inelastic deformation in estimating changes in in situ stress, strain and stored elastic strain energy—in the context of investigating induced seismicity in the Groningen gas field and other similar fields.

2. Background on the Slochteren Sandstone

The Groningen gas field is a vast ~30 by 30 km field located in the NE-Netherlands (Figure 1). The ~100- to 200-m thick Slochteren reservoir sandstone member is located at about 3-km depth and constitutes coarse, poorly sorted fluvial sandstones and conglomerates at its base, superseded by cross-bedded, intermediate- to well-sorted aeolian sandstones (Grotsch et al., 2011). The Slochteren sandstone lies unconformably on organic-rich Carboniferous shales and is overlain by a 50-m thick claystone, followed by a thick sequence (500–1,000 m) of Zechstein evaporates (Amthor & Okkerman, 1998). At present, the upper 50–150 m of the Slochteren reservoir is gas bearing and is partly (25 ± 10 vol%) filled with connate brine (Waldmann, 2011). Production from the field started in 1963, which has led to a decrease in pore pressure from 35 MPa to ~8 MPa, in 2016 (NAM, 2016). This has resulted in an upward shift of the gas-water contact by about 10 m, to a current true vertical depth of ~2,971 m. The sandstone is quartz rich (72–90 vol%), with lesser amounts of feldspar (8–25 vol%), clay (0.5–5.5 vol%), and lithic fragments (3–10 vol%), which include basaltic and sedimentary lithoclasts (Waldmann et al., 2014; Waldmann & Gaupp, 2016). The mean size of quartz and feldspar grains typically ranges between 150 and 250 μm (Pijnenburg et al., 2018). Clay films (1- to 10- μm thick) coat the surfaces of quartz and feldspar grains and many grain contacts (Gaupp et al., 1993; Waldmann, 2011; Waldmann & Gaupp, 2016; Wilson, 1992). The porosity of the Slochteren sandstone is well constrained from wireline logs and fluid-immersion tests on core plugs (NAM, 2013), with average values decreasing from 18% to 22% in the center of the field to 12%–16% at the margins (Figure 1b).

3. Experimental Aspects

We performed two types of experiments on Slochteren sandstone plugs from the Groningen gas reservoir: (1) purely hydrostatic stress cycling tests (hydrostatic experiments) and (2) hydrostatic followed by deviatoric stress cycling tests (combined hydrostatic plus deviatoric experiments). Both experiment types were aimed at systematically investigating the elastic versus inelastic stress-strain and porosity reduction behavior of the material, as a function of initial porosity. We explored hydrostatic mean effective stresses up to 320 MPa and differential stresses up to 135 MPa, at a temperature of 100 °C, representative for the Groningen field temperature at 3,000-m true vertical depth (NAM, 2013). A constant pore pressure of either 0.1 or 1 MPa was used. These stress conditions were chosen to cover all stages of $P-\Delta\phi_t$ behavior commonly seen in sandstones (Figure 2; Wong & Baud, 2012), and include the effective confining pressures and differential stresses relevant for fluid extraction from reservoirs at depths up to 5 km (both typically <50 MPa; Schutjens et al., 2004). In addition, a set of reference experiments was performed to investigate microstructural changes specific to each stage of deformation. During hydrostatic stress cycling runs, we imposed a rate of change of mean effective stress (\dot{P}) of 0.1 ± 0.05 MPa/s. During deviatoric stress cycling, a total axial strain rate $\dot{\epsilon}_t$ of 10^{-5} s^{-1} was used, leading to a similar rate of change of the mean effective stress.

3.1. Sample Material and Pore Fluid Chemistry

The samples used were obtained from Slochteren sandstone core, retrieved by the field operator (NAM) from the Zeerijp (ZRP)-3a well in 2015. Sets of six adjacent samples were extracted from 10-cm diameter core sections obtained from five different depth intervals characterized by different porosities (Table 1), in an orientation perpendicular (within $\sim 10^\circ$) to the often slightly inclined bedding. Each sample set consisted of four uniformly looking, 25.4-mm diameter cylindrical plugs cored with a length of 55 to 65 mm, one smaller cylindrical plug cored with a diameter of 9.8 mm and a length of 20 mm, one sample of “interplug” material with an equivalent diameter of ~20 mm, and a length of 55 to 65 mm left over after drilling. The interplug samples (no suffix used in Table 1) were left undeformed and were used as a benchmark to determine experimentally induced microstructural changes. The ends of all cylindrical plugs were ground flat and perpendicular to the long sample axis using a polishing wheel and support block.

Table 1
List of the Samples Used and Key Mechanical Data Obtained in the Present Study

Sample	TVD (m)	φ_0 (%)	Test type	$(P_c^{\text{eff}})_{\text{max}}$ (MPa)	Q_{peak} (MPa)	P_{stage3d} (MPa)	P_{stage3c} (MPa)	$\Delta\varphi_{i,\text{stage3d/c}}$ (%)	$\Delta\varphi_{i,\text{fin}}$ (%)	$\Delta\varphi_{i,\text{fin}}$ (%)	$\bar{\rho}_{cr}$ (mm^{-2})
<i>Control experiments: ($\varphi_0 = 19.1\%$)</i>											
z74a	2,968.9	19.1 ^X	T	40.0	79.5		65	0.9	2.70	1.42	<i>n.d.</i>
z74b ^a	2,968.9	19.1	T	40.0	82.7		65	<i>n.d.</i>	2.67	1.39	<i>n.d.</i>
<i>Low porosity samples: ($\varphi_0 = 13.4\%$ to 13.9%)</i>											
z20	2,939.6	13.4	U								5.4
z20a	2,939.6	13.4 ^X	T	5.0	49.5	11		0.2	−0.39	−0.13	<i>n.d.</i>
z20d	2,939.6	13.4	T	20.0	83.7	43		0.5	0.97	0.43	<i>n.d.</i>
z20c	2,939.6	13.4	T	40.0	113.0	75		0.7	1.64	0.62	33.5
z20b	2,939.6	13.4	T	80.0	134.4		117	1.0	3.33	1.28	<i>n.d.</i>
z20e ^b	2,939.6	13.9 ^X	R	320	<i>n.a.</i>		220	1.3	7.4	3.2	<i>n.d.</i>
<i>Intermediate porosity samples: ($\varphi_0 = 21.4\%$ to 21.5%)</i>											
z24	2,960.6	21.5	U								8.4
z24b	2,960.6	21.5	T	5.0	29.7	9		0.2	−0.39	0.05	10.0
z24d	2,960.6	21.5	T	20.0	53.8	32		0.7	1.63	0.78	14.0
z24c	2,960.6	21.5	T	40.0	70.4		60	0.9	3.17	1.58	38.7
z24a ^b	2,960.6	21.5 ^X	T	80.0	<i>n.d.</i>		93	1.0	3.82	1.32	23.5
z24e ^b	2,960.6	21.4 ^X	R	160	<i>n.a.</i>		130	1.1	5.5	2.1	72.8
<i>High porosity samples: ($\varphi_0 = 25.6\%$ to 26.4%)</i>											
z84	3,014.5	26.4	U								11.5
z84a	3,014.5	26.4 ^X	T	5.0	22.1	7		0.2	−0.18	0.12	<i>n.d.</i>
z84d	3,014.5	26.4	T	20.0	39.1	34		1.0	2.22	1.12	<i>n.d.</i>
z84c	3,014.5	26.4	T	40.0	43.5		53	1.3	3.45	1.83	25.7
z84b ^b	3,014.5	26.4	T	80.0	<i>n.d.</i>		86	1.7	5.70	3.18	<i>n.d.</i>
z84e ^b	3,014.5	25.6 ^X	R	160	<i>n.a.</i>		125	1.8	5.8	2.5	<i>n.d.</i>
<i>Microstructural reference experiments: ($\varphi_0 = 21.9\%$)</i>											
z77	2,977.0	21.9	U								12.8
z77a ^a	2,977.0	21.9 ^X	T	40.0	<i>n.a.</i>		<i>n.d.</i>	<i>n.d.</i>	2.37	1.24	14.2
z77b ^a	2,977.0	21.9	T	40.0	<i>n.d.</i>		<i>n.d.</i>	<i>n.d.</i>	2.72	1.35	17.7
z77c ^a	2,977.0	21.9	T	40.0	59.1		58	<i>n.d.</i>	3.10	1.68	54.3

Note. TVD refers to the true vertical depth within the Zeerijp (ZRP)-3a well, from which our samples were recovered. φ_0 denotes the initial porosity (measured value indicated with ^X—values of twin samples assumed to be equal); $(P_c^{\text{eff}})_{\text{max}}$ denotes the maximum effective confining pressure imposed on each sample; Q_{peak} denotes the differential stress ($\sigma_1 - \sigma_3$) at failure, that is, at the onset of strain-softening behavior. P_{stage3d} and P_{stage3c} indicate the mean effective stress beyond which Stage 3d (nonlinear and dilatant—see Figure 2) and Stage 3c behavior (nonlinear and compactant) was seen, while $\Delta\varphi_{i,\text{stage3d/c}}$ refers to the corresponding inelastic porosity reduction. $\Delta\varphi_{i,\text{fin}}$ denotes the final total porosity reduction measured before the final unloading stage. $\Delta\varphi_{i,\text{fin}}$ denotes the final, inelastic porosity reduction measured at the end of each test after full unloading to the initial P of 5 MPa and Q of 0 MPa. $\bar{\rho}_{cr}$ denotes the mean crack density, defined as the number of cracks per mm^2 obtained in backscattered electron images. U, T, and R indicate whether the sample was left undeformed (U) or else was tested in hydrostatic plus deviatoric compression in the triaxial vessel (T) or in purely hydrostatic compression in the Rene vessel (R).

^aMonotonic loading without stress cycling. ^bNo strain-softening observed.

The four longer plugs were used in our hydrostatic plus deviatoric experiments and are annotated with suffixes “a–d” (Table 1). These experiments were performed using a highly saline pore fluid with ion concentrations of 3.4 M Na^+ , 0.1 M K^+ , 1.0 M Ca^{2+} , 0.2 M Mg^{2+} , 0.6 M SO_4^{2-} , and 5.7 M Cl^- , similar to those measured in pore fluid sampled from the reservoir see supporting information S1 and Hol et al., (2018). All samples were presaturated with this pore fluid prior to testing. We determined the initial porosity of one 25.4-mm diameter sample from each set, using the difference in mass between the washed and dried sample versus that of the sample saturated with the above brine (density = 1.21 g/mL). The values obtained for the samples selected from each set were 13.4%, 19.1%, 21.5%, 21.9%, and 26.4% (Table 1). These porosities were assumed to be representative for the other long twin plugs and for the interplug sample, in each set (each core interval with given average porosity). This assumption is justified by previous testing of Slochteren sandstone samples from ZRP-3a core, showing similar physio-mechanical properties of samples from the same core interval (Hol et al., 2018).

Three of the short, 9.8-mm diameter plugs, taken from the depth intervals with long sample porosities of 13.4%, 21.5%, and 26.4% were used for (purely) hydrostatic tests. These samples are identified with the suffix “e” (Table 1). After drilling (supporting information S1), they were dried. Hydrostatic experiments were performed at 50% pore fluid saturation and the same ion concentration as used in combined hydrostatic plus

deviatoric tests. This was achieved by first saturating the short samples in full using 50% diluted brine. The mass difference between dry and saturated sample was used to determine the initial porosity, yielding similar values to those obtained for the long samples from the same depth interval, notably 13.9%, 21.4%, and 25.6% (Table 1). Prior to testing, the diluted pore fluid was allowed to evaporate to 50% saturation, using a mass balance.

3.2. Experimental Apparatus

The deformation machines used in this study are described in detail in the supporting information S2 (Peach, 1991; Pijnenburg et al., 2018). In short, the combined hydrostatic plus deviatoric stress cycling experiments were performed using an externally heated, constant volume triaxial testing machine. This triaxial machine is capable of operating at servo-controlled confining pressures up to 100 MPa, while axial (deviatoric) loading up to differential stresses of 800 MPa is achieved through motor-driven advancement of a yoke plus loading piston assembly at constant displacement rate.

Given the confining pressure limitations of the above triaxial apparatus, a second, higher pressure apparatus was employed for the purely hydrostatic stress cycling tests, to ensure that Stage 3c behavior could be accessed in hydrostatic compression. This apparatus, referred to here as the Rene vessel, consisted of an externally heated, cold seal, 400-MPa pressure vessel made of Rene 41 super alloy, having an inner and outer diameter of 12 and 51 mm and containing a sealed cylindrical sample assembly (see supporting information S2). Water was used as the confining medium and pressure was applied to the sample using a 400 MPa, manually operated, Nova syringe pump. Pore fluid access to the sample is not possible using this apparatus. Hydrostatic tests were accordingly performed under undrained conditions, using samples incompletely-saturated with water vapor at the testing temperature and pore pressure, to buffer the pore fluid pressure at a value of $P_p \approx 0.1$ MPa under test conditions, that is, at confining pressures up to 320 MPa and a temperature of 100 °C.

3.3. Sample Assembly and Experimental Procedure

3.3.1. Combined Hydrostatic Plus Deviatoric Experiments

These tests employed the samples prepared with a diameter of 25.4 mm. In setting up each run, the sample was removed from its brine-filled container and jacketed between an upper and lower loading blocks using a fluorinated ethylene propylene sleeve. To reduce friction at the sample/end-block interface, a double layer consisting of two perforated Teflon sheets (50 μ m) was included at each end of the sample. After tourniquet sealing, the sample assembly was emplaced into the pressure vessel. The confining pressure was increased to 5 MPa. The pore fluid system was evacuated for 15 min, followed by application of the required pore pressure ($P_p = 1$ MPa) and confining pressure ($P_c = 6$ MPa), resulting in an effective confining pressure ($P_c^{\text{eff}} = P_c - P_p$) of 5 MPa. The sample was then brought to the desired testing temperature ($T = 100$ °C), while maintaining P_c^{eff} below the initial effective value of 5 MPa used during the test. The sample and vessel were left to equilibrate to these pressure and temperature conditions for 4 hr.

Upon P - T equilibration, samples were either maintained at $P_c^{\text{eff}} = 5$ MPa (the lowest value for subsequent axial stress cycling), or else subjected to hydrostatic stress cycling, at constant pore pressure, until an effective confining pressure of 20, 40, or 80 MPa was reached (the target value for subsequent axial stress cycling). During hydrostatic stress cycling, the confining pressure was increased at a constant rate \dot{P} of ~ 0.1 MPa/s to maximum values that were incremented by 5 MPa in each successive cycle. Each pressurization step was followed by depressurization to the initial P_c^{eff} value of 5 MPa, to determine any inelastic (permanent) pore volume changes. Upon achieving the target confining pressure and P_c^{eff} value for axial stress cycling (5, 20, 40, or 80 MPa), P_c^{eff} was held constant and axial stress cycling initiated. To achieve axial stress cycling, we repeatedly loaded and unloaded the sample up to differential stress ($\sigma_1 - \sigma_3$) values that were successively increased by 5 MPa (at $P_c^{\text{eff}} = 5$ MPa), or by 10 MPa (at $P_c^{\text{eff}} = 20, 40, \text{ or } 80$ MPa). Each uploading step was followed by full piston retraction (i.e., $[\sigma_1 - \sigma_3] = 0$ MPa), to measure the amount of permanent deformation developed in the foregoing stress cycle. Loading and unloading was performed by applying a near-constant total axial strain rate ($\dot{\epsilon}_t$) of $\sim 10^{-5}$ s $^{-1}$, which for the present samples led to an equivalent \dot{P} of 0.1 ± 0.05 MPa/s (as imposed during hydrostatic cycling). This procedure was repeated until the sample showed strain-softening behavior (i.e., failure), strain-neutral behavior, or a combination of decreasing strain-hardening rates and strongly nonlinear, enhanced porosity reduction (i.e., a clear deviation from (quasi-)linear force

versus pore fluid volume change behavior). Subsequently, each sample was axially unloaded ($[\sigma_1 - \sigma_3] = 0$ MPa) and depressurized to $P_c^{\text{eff}} = 5$ MPa. The sample was maintained at these conditions for several minutes to ensure a constant pore volume signal. Finally, the pore pressure was removed, followed by full reduction of the confining pressure, and the furnace was switched off. After cooling to ~ 80 °C, the sample assembly was removed from the testing machine.

To assess the effect of cyclic hydrostatic plus deviatoric loading on sample behavior, as opposed to monotonic loading, we performed a set of two control experiments on directly adjacent twin samples taken from the same core section (z74a and z74b; $\varphi_0 = 19.1\%$; see Table 1). One sample (z74b) was monotonically loaded and unloaded, without hydrostatic or deviatoric stress cycling, while the other was stress cycled. The hydrostatic and deviatoric loading/unloading stages of both experiments were performed respectively up to- and at an effective confining pressure P_c^{eff} of 40 MPa, using the same baseline P_c^{eff} of 5 MPa, and the same conditions of P_p , T , \dot{P} , $\dot{\epsilon}_t$, and pore fluid chemistry, as employed in all other experiments.

In addition, a set of three microstructural reference experiments was performed on samples with an initial porosity of $\varphi_0 = 21.9\%$ (Table 1), to investigate permanent microstructural changes occurring during loading to the point of strain-softening, that is, failure. In these experiments, we imposed hydrostatic compression to a P_c^{eff} of 40 MPa (sample z77a), followed by deviatoric compression reaching Q values up to 50 MPa (sample z77b), followed by deviatoric compression to failure at Q values > 50 MPa (sample z77c). In each case, loading and unloading were performed monotonically to generate reference microstructures for the same stages of deformation explored in load-cycled samples. All other conditions were identical to the main body of tests.

3.3.2. Hydrostatic Experiments

For these purely hydrostatic tests, we used the (400 MPa) Rene vessel and samples with a diameter of 9.8 mm. To ensure a constant pore pressure of 0.1 MPa throughout testing under undrained conditions (see section 3.2), these tests were performed using 50 vol% saturated samples (see section 3.1). Each sample was jacketed using a fluorinated ethylene propylene sleeve and sealed between stainless steel endpieces. Sealing was achieved using wire tourniquets tightened onto underlying EPDM rubber rings, countersunk into the endpieces. The sample was subsequently emplaced in the fluid-filled pressure vessel and pressurized at 3–5 MPa. The temperature was then raised to 100 °C over 17 hr, while maintaining the confining pressure roughly constant. Upon temperature equilibration, P_c was raised to 5.1 MPa, while assuming that the pore pressure remained constant at 0.1 MPa due to partial saturation.

The confining pressure was then increased in 5-MPa steps, again assuming constant P_p . This was achieved by stepwise injection of confining fluid, leading to an increase in P_c of 5 MPa within 15 ± 2 s, in each step. Following each 5-MPa pressure step, the confining pressure was held constant for 30 s to allow manual reading of the instantaneous confining pressure, the injected confining fluid volume, and the temperature. The resultant average rate of change of the confining pressure per step was approximately 0.1 ± 0.02 MPa/s. Hydrostatic compression was continued until an effective confining pressure of 20 MPa was reached. At this stage, P_c was lowered in the same 5-MPa steps to the initial value of 5.1 MPa, to allow for measurement of any inelastic volume changes. At this pressure, the confining pressure was held constant for 15 min, in order to ensure full P - T equilibration of the confining fluid volume. No or negligible change in P_c was observed, implying that the pressurization rate was sufficiently low to allow P - T equilibration of the confining fluid during successive loading/unloading cycles.

In subsequent stress cycles, this procedure was repeated, incrementing the maximum effective confining pressure imposed by 20 MPa in each cycle. The procedure was continued until a clear deviation from near-linear confining pressure versus injected fluid volume behavior was observed. Upon completion of the experiment, the temperature was lowered to $T \sim 80$ °C, the residual confining pressure of 5.1 MPa was removed, and the sample was extracted from the vessel.

3.4. Data Acquisition and Processing

We adopt the convention that compressive stress, compressive axial strain, and porosity reduction (i.e., compaction) are positive.

3.4.1. Combined Hydrostatic Plus Deviatoric Experiments

In these experiments, the internal axial load, confining pressure, pore pressure, pore fluid volume change, sample temperature, and axial displacement signals were logged at 2 Hz, using a 16-bit DAQPad National

Instruments A/D converter. After correcting for apparatus distortion and thermal pore fluid volume changes during flow in and out of the vessel (cf. Pijnenburg et al., 2018), these data were processed to yield the differential stress ($Q = \sigma_1 - \sigma_3$), the mean effective stress (P), the total axial strain $\epsilon_t \approx e_t$ (small change in sample length/the initial sample length) and the total porosity reduction $\Delta\phi_t$ (change in sample pore volume/divided by the initial sample volume) versus time. The peak strength (Q_{peak}) is defined as the maximum differential stress supported by a given sample before failure (i.e., strain-softening behavior) was observed.

The elastic behavior of the samples was quantified using the reversible behavior observed during the unloading stages of the hydrostatic and deviatoric load cycles. The bulk modulus (K) and Young's modulus (E) were determined at target mean effective stresses (P) of 10, 30, 50, and 85 MPa, by linear regression of the first P versus $\Delta\phi_t$ unloading data and Q versus ϵ_t unloading data, respectively, both obtained within ± 2.5 MPa of the target P value. The error in K and E resulting from linear regression analysis in the combined hydrostatic and deviatoric experiments lay within 1% of the determined values.

The inelastic (permanent) change in pore volume accumulated during stress cycling was obtained from the difference between the pore volumes measured at the start and end of each loading cycle, whether hydrostatic or deviatoric. The inelastic porosity reduction ($\Delta\phi_i$) accumulated in successive cycles was determined from the sum of the permanent pore volume changes measured per cycle, divided by the initial (pretest) sample volume V_0 . For the small porosity reductions measured in this study, the use of V_0 as reference state, rather than the incremental sample volume, resulted in relative errors in $\Delta\phi_i$ of $<5\%$. The inelastic axial strain was determined for each deviatoric stress cycle by dividing the permanent change in sample length determined upon axial unloading, referenced to the sample length measured at the first axial loading stage, by the initial sample length L_0 .

3.4.2. Hydrostatic Experiments

In the purely hydrostatic stress cycling experiments performed in the Rene vessel, the confining pressure, confining fluid volume, and vessel temperature data were recorded manually upon each 5 MPa change of the confining pressure. Confining fluid volume data were obtained by recording the number of syringe pump rotations required to introduce a given confining pressure. The accuracy of this measurement was $\pm 0.2 \mu\text{L}$. The resulting volumetric data were corrected for distortion of the pressure vessel, using predetermined calibrations, and for thermal volume changes of the confining fluid during flow in and out of the heated pressure vessel. The corrected sample volume data (ΔV_s) were subsequently used to calculate total porosity reduction ($\Delta\phi_t \approx \epsilon_{v,t} = \Delta V_s/V_0$; accuracy $\pm 0.03\%$) versus confining pressure change and time. Thus, for the purpose of presenting and comparing the results in the first instance, we assume that the pore and bulk volume responses are equal. The data later demonstrate that this is a good approximation. For each unloading stage, K was determined at target mean effective stresses of 30, 50, and 85 MPa and in a similar manner to that used in the combined hydrostatic plus deviatoric experiments but employing a mean effective stress range of ± 15 MPa to compensate for the lower data sampling frequency. The error in K resulting from linear regression analysis of our hydrostatic stress cycling data was $\pm 10\%$ of the determined value. The inelastic porosity reduction ($\Delta\phi_i$) occurring in each stress cycle was determined by dividing the permanent change in sample volume, determined after hydrostatic unloading to the starting effective confining pressure of 5 MPa, by the initial sample volume V_0 .

3.5. Microstructural Analysis

To investigate the distribution of intragranular cracks in the deformed versus undeformed samples and hence to assess any tendency for localization of brittle deformation, we performed quantitative microstructural analysis of crack density on all 21.9% porosity samples used in microstructural reference tests (z77a–z77c), all 21.4%–21.5% porosity samples used in hydrostatic and hydrostatic plus deviatoric stress cycling tests (z24a–z24e), and the 13.4% (z20c) and 26.4% (z84c) porosity samples, tested in the hydrostatic plus deviatoric stress cycling tests performed at a maximum effective confining pressure of 40 MPa. The undeformed counterparts of these samples were also analyzed. Deformed samples were extracted from the relevant apparatus; the jacket was removed, and the brine was replaced by demineralized water by soaking the sample in demineralized water for 6–7 days. After drying, the deformed and undeformed samples were impregnated with Araldite 2020 resin, sectioned, and imaged in full using a FEI Helios Nanolab G3 Focused Ion Beam scanning electron microscope operated in backscatter electron (BSE) mode (see

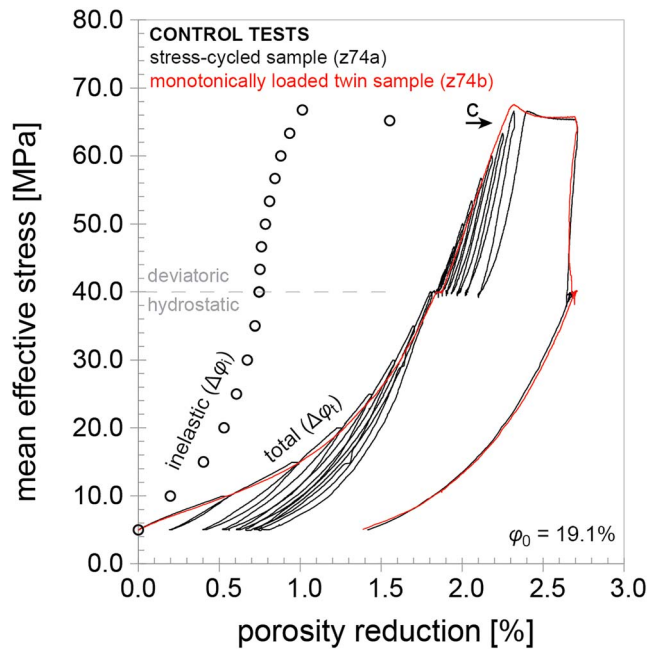


Figure 3. Plot showing mean effective stress (P) versus total porosity reduction ($\Delta\phi_t$) and inelastic porosity reduction data ($\Delta\phi_i$) obtained for stress-cycled sample z74a, alongside the P - $\Delta\phi_t$ data obtained during monotonic loading and final unloading of twin sample z74b. In both cases, hydrostatic compression up to $P = 40$ MPa was followed by axial compression at constant effective confining pressure. The arrow and annotation “c” indicate the onset of Stage 3c behavior (cf. Figure 2) in both samples. The stress-cycled sample (z74a) demonstrates inelastic (permanent) compaction throughout compression. Both samples show very similar P - $\Delta\phi_t$ behavior, implying negligible damaging of samples by stress cycling.

P - $\Delta\phi_t$ behavior up to $P \approx 35$ MPa, followed by near-linear behavior up to $P \approx 65$ MPa. Within the near-linear region, the total hardening rate (i.e., the slope $dP/d\Delta\phi_t$) was 5.8 GPa. At $P > 65$ MPa, this rate decreased toward peak strengths of $P = 66.5$ MPa (z74a; $Q_{\text{peak}} = 79.5$) and 67.5 MPa (z74b; $Q_{\text{peak}} = 82.7$ MPa) reached at $\Delta\phi_t \approx 2.3\%$, followed by strain-softening and then strain-neutral behavior, reached at $\Delta\phi_t \approx 2.5\%$. Upon unloading, the samples again displayed closely similar P - $\Delta\phi_t$ behavior, yielding near-identical final inelastic porosity reductions ($\Delta\phi_{i,\text{fin}}$ —Table 1) of $1.4\% \pm 0.02\%$ at the reference P value of 5 MPa. Note that the stress-cycled sample z74a showed inelastic porosity reduction after every stress cycle, as shown by the open circle data points in Figure 3. Note also the S-shaped curve defined by these data, with a more or less constant inelastic hardening rate (i.e., the slope $dP/d\Delta\phi_i$) of approximately 14 GPa characterizing the stress interval between $P \approx 35$ MPa and 65 MPa.

4.2. Mechanical Data for Low, Intermediate, and High-Porosity Sample Sets

4.2.1. Combined Hydrostatic Plus Deviatoric Test Data

Figure 4 shows the mechanical data obtained during the combined hydrostatic plus deviatoric stress cycling experiments performed on the low ($\phi_0 = 13.4\%$), intermediate ($\phi_0 = 21.5\%$), and high porosity ($\phi_0 = 26.4\%$) sample sets listed in Table 1.

All samples showed typical Stages 1, 2, 3d, and 3c mean effective stress (P) versus total porosity reduction ($\Delta\phi_t$) behavior of the type often described in the literature (compare Figures 4a–4c with Figure 2). At the lowest effective confining pressure tested ($P_c^{\text{eff}} = 5$ MPa), samples showed a transition from initial, nonlinear, concave-up behavior (cf. Stage 1, in Figure 2) to nonlinear, dilatant behavior (Stage 3d), at mean effective stresses (P_{stage3d} —indicated by arrows and annotation d in Figures 4a–4c; see also Table 1) ranging from 7 (high initial porosity) to 11 MPa (low initial porosity). At these low values of P_c^{eff} , near-linear Stage 2 behavior was not seen. All other tests ($P_c^{\text{eff}} \geq 20$ MPa) showed Stage 1 behavior up to $P \approx 35$ MPa, followed by

supporting information S3; Preibisch et al., 2009; Sakic et al., 2011). The undeformed microstructural reference sample (z77) was analyzed further using electron dispersive X-ray spectrometry (EDX), to produce element maps.

The analyses were conducted along an axial profile traversing the full length of each sample studied, using stitched, BSE micrographs. For each sample, we analyzed a 1-mm wide strip, manually outlining each visible crack using ImageJ software. Thus, in each sample a total area of 20 to 65 mm² was analyzed (containing ~ 800 –3,000 grains), depending on the length of the sample investigated. From these data, crack densities, defined as the number of intragranular cracks per mm², were obtained as a function of position along the length of each sample. Mean crack densities ($\bar{\rho}_{cr}$) and the standard deviation (SD) of the crack density distribution were also computed.

4. Stress Cycling Test Results

In addition to the basic sample data, Table 1 lists the experiments performed, the corresponding experimental conditions, and key items of the mechanical and microstructural data obtained.

4.1. Control Experiments: Stress Cycling Versus Monotonic Loading Behavior

The mean effective stress (P) versus total porosity reduction ($\Delta\phi_t$) data obtained during the hydrostatic plus deviatoric stress cycling experiment performed on sample z74a ($\phi_0 = 19.1\%$) are presented in Figure 3, alongside the monotonic loading and then unloading data obtained for twin sample z74b. Both samples were subjected to hydrostatic compression up to $P_c^{\text{eff}} = 40$ MPa, followed by deviatoric compression at constant P_c^{eff} . Despite the cyclic versus monotonic loading paths, the P - $\Delta\phi_t$ behavior shown by both samples is very similar. Both exhibit concave-up

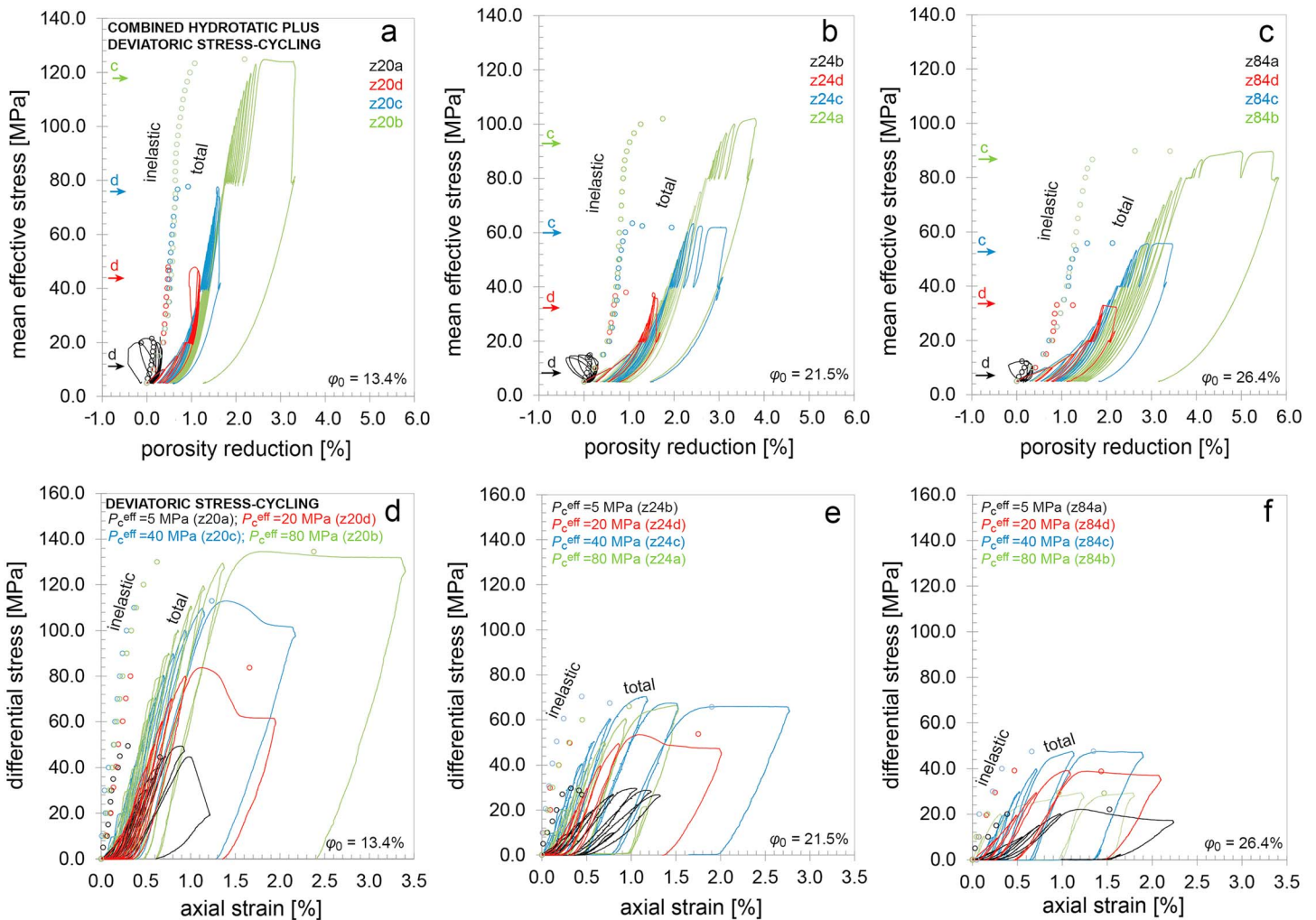


Figure 4. Plots showing the mechanical data obtained in our combined hydrostatic plus deviatoric stress cycling experiments performed in the triaxial vessel on samples with low ($\phi_0 =$ of 13.4%; left column), intermediate ($\phi_0 = 21.5\%$; middle column), and high initial porosities ($\phi_0 = 26.4\%$; right column). Here hydrostatic stress cycling up to effective confining pressures (P_c^{eff}) of 5, 20, 40, and 80 MPa was followed by deviatoric stress cycling at constant P_c^{eff} . (a–c) Mean effective stress versus total ($\Delta\phi_t$; solid curves) and inelastic porosity reduction data ($\Delta\phi_i$; open circles). For all initial porosities explored here, the P – $\Delta\phi_t$ and P – $\Delta\phi_i$ data obtained show a typical sequence of initial Stages 1 (nonlinear and concave-up), 2 (near linear), and 3d (nonlinear and dilatant) or 3c (nonlinear and compactant) behavior (compare with Figure 2). Arrows “d” and “c” indicate the onset of Stages 3d or 3c, respectively. Inelastic porosity reduction is seen during all stages, including the near linear Stage 2, which is often assumed to reflect poroelasticity. (d–f) Plots showing differential stress Q versus total (ϵ_t ; solid curves) and inelastic axial strain (ϵ_i ; open circles) data. Enlargements of this figure are included in the supporting information.

near-linear P – $\Delta\phi_i$ behavior (Stage 2). During this near-linear stage, the total hardening rate (i.e., $dP/d\Delta\phi_t$) decreased with increasing initial porosity, yielding 8.3 ± 0.5 GPa in low porosity sandstones, 5.7 ± 0.4 GPa at intermediate porosities, and 4.1 ± 0.5 GPa in high porosity samples. These Stage 2 hardening rates were similar in both hydrostatic and deviatoric loading, implying isotropic behavior. For all samples tested at $P_c^{\text{eff}} = 20$ MPa and the low porosity sample tested at $P_c^{\text{eff}} = 40$ MPa, deviation from these near-linear trends was characterized by dilation (Stage 3d). At higher P_c^{eff} and initial porosity, our samples showed nonlinear compaction (Stage 3c, marked by P_{stage3c} in Table 1). The inelastic porosity reductions ($\Delta\phi_{i,\text{stage3d/c}}$) at these dilatant and compactant deviations from linearity are listed in Table 1.

Inelastic porosity reduction ($\Delta\phi_i$; open circles in Figure 4) was observed after every hydrostatic and deviatoric stress cycle, in all experiments. The P – $\Delta\phi_i$ behavior was qualitatively similar to that shown by P – $\Delta\phi_t$ data, showing a transition from Stages 1 to 3d behavior at the lowest P_c^{eff} of 5 MPa and from Stages 1 to 2 and ultimately Stage 3c behavior at higher P_c^{eff} (Figures 4a–4c). However, for each stage, the observed P – $\Delta\phi_i$

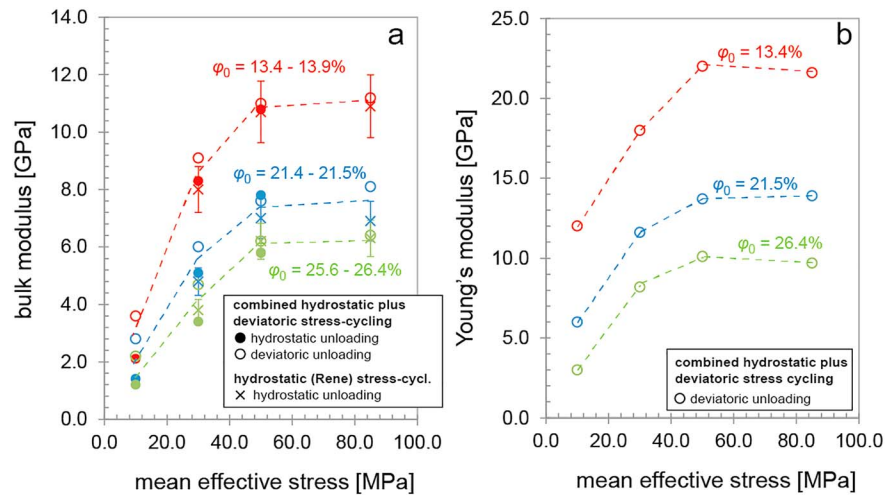


Figure 5. Plots showing (a) bulk modulus (K) and (b) Young's modulus (E) versus mean effective stress (P) data, obtained using both hydrostatic and deviatoric unloading data of combined hydrostatic plus deviatoric experiments performed in the triaxial vessel on samples with low ($\varphi_0 =$ of 13.4%), intermediate ($\varphi_0 =$ of 21.5%), and high initial porosities ($\varphi_0 =$ of 26.4%). K values are compared to the bulk moduli obtained from the unloading curves of the hydrostatic experiments performed in the Rene vessel (see Figure 6), using samples with similar φ_0 of 13.9%, 21.4%, and 25.6%. Note that K values obtained using the hydrostatic unloading data obtained in the Triaxial vessel versus those obtained in the Rene vessel are similar within the error in the K values determined using Rene vessel data.

behavior was stiffer by a factor of 1.5 to 3. During Stage 2, inelastic hardening rates were found to be 27.8 ± 1.2 GPa (low φ_0), 16.7 ± 0.7 GPa (intermediate φ_0), and 9.8 ± 0.5 GPa (high φ_0). These rates were again found to be similar for both hydrostatic and deviatoric stress cycles.

During the deviatoric stages of the combined hydrostatic plus deviatoric experiments, differential stress (Q) versus total axial strain (ε_t) and inelastic axial strain (ε_i) data showed S-shaped behavior, where nonlinear $Q-\varepsilon_t$ and ε_i behaviors transitioned into near-linear strain hardening trends at $Q > 5$ to 10 MPa (Figures 4d–4f). These near-linear $Q-\varepsilon_t$ and ε_i trends were followed by strain hardening at a decreasing rate, which, in most of our samples, led to a peak strength (Q_{peak} ; listed in Table 1) followed by strain-softening (i.e., failure). However, in the more porous samples ($\varphi_0 \geq 21.5\%$), deviatorically compressed at the highest P_c^{eff} of 80 MPa, the peak strength was not attained and strain hardening continued at decreasing rates to the end of the experiment. Where attained, peak strength values increased with increasing P_c^{eff} and with decreasing φ_0 (Table 1). The final inelastic porosity reductions attained in each experiment are listed in Table 1.

Bulk moduli (K) determined from both hydrostatic and deviatoric unloading data and the Young's moduli (E) obtained from deviatoric unloading data are plotted versus the mean effective stresses (P) of 10, 30, 50, and 85 MPa at which K and E were determined, in Figure 5. Both K (Figure 5a) and E (Figure 5b) increase with increasing P and decreasing φ_0 , reaching constant values at $P \geq 50$ MPa. At $P \leq 30$ MPa, bulk moduli obtained in deviatoric unloading stages are higher by 1 to 2 GPa than the corresponding hydrostatic values (Figure 5a). By contrast, at $P \geq 50$ MPa, deviatoric and hydrostatic K values are similar to within 0.3 GPa.

4.2.2. Hydrostatic Test Data (Rene Vessel)

The mean effective stress (P) versus total ($\Delta\varphi_t$) and inelastic porosity reduction ($\Delta\varphi_i$) data obtained in the purely hydrostatic experiments performed in the Rene vessel on our low ($\varphi_0 = 13.9\%$), intermediate ($\varphi_0 = 21.4\%$), and high porosity ($\varphi_0 = 25.6\%$) samples are presented in Figures 6. The P versus $\Delta\varphi_t$ and $\Delta\varphi_i$ curves obtained for each sample (i.e., each porosity) show S-shaped behavior, again reflecting evolution from Stages 1 to 2 and ultimately Stage 3c behavior (cf. Figure 2). Nonlinear, concave-up Stage 1 behavior was seen up to $P \approx 35$ MPa, followed by a near-linear Stage 2 trend (Figure 6). During Stage 2, the total and inelastic hardening rates were roughly similar to those obtained in the Stage 2 intervals of combined hydrostatic plus deviatoric tests, yielding $dP/d\Delta\varphi_t$ values of 7.5 GPa (low φ_0), 5.7 GPa (intermediate φ_0), and 4.1 GPa (high φ_0) while the $dP/d\Delta\varphi_i$ values were 25.4, 17.0, and 11.3 GPa, respectively. In the low porosity sample, this near-linear behavior persisted up to $P \approx 220$ MPa, beyond which hardening rates gradually

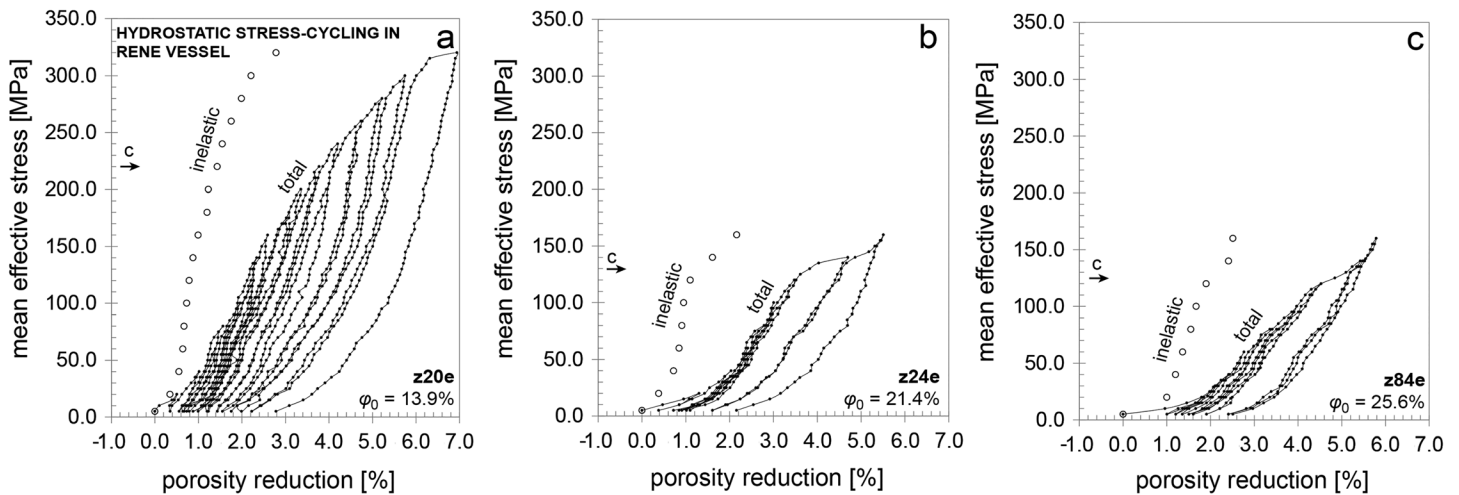


Figure 6. Plots showing mean effective stress (P) versus total ($\Delta\varphi_t$) and inelastic porosity reduction ($\Delta\varphi_i$) data obtained in our purely hydrostatic stress cycling experiments performed in the Rene vessel on samples with (a) low ($\varphi_0 = 13.9\%$), (b) intermediate ($\varphi_0 = 21.4\%$), and (c) high initial porosities ($\varphi_0 = 25.6\%$). These samples were obtained from the same depth interval as the samples used in the stress cycling experiments shown in Figure 4. P - $\Delta\varphi_t$ and P - $\Delta\varphi_i$ data show typical Stages 1 (nonlinear and concave up), 2 (near linear), and 3c (nonlinear and concave down) behavior (cf. Figure 2). Arrows indicate the onset of Stage 3c behavior in each experiment (P_{stage3c} ; Table 1).

decreased (Stage 3c) leading to a marked inelastic porosity reduction of 0.6% in the P interval of 315 to 320 MPa (Figure 6a). Higher porosity samples showed nonlinear, concave-down compaction (Stage 3c) in the P intervals of 130 to 150 MPa ($\varphi_0 = 21.4\%$; Figure 6b) and of 125 to 140 MPa ($\varphi_0 = 25.6\%$; Figure 6c), beyond which the samples hardened at increasing rates up to the highest P of 160 imposed. Note that aside from the similar hardening rates shown during Stage 2, the values of $\Delta\varphi_t$ and $\Delta\varphi_i$ determined at given mean effective stress and initial porosity values are similar within $\sim 10\%$ to the values measured during the hydrostatic stages of our combined hydrostatic plus deviatoric experiments (see Figures 4a–4c), at least up to the highest hydrostatic P of 80 MPa explored in the latter.

Bulk moduli (K) determined from our hydrostatic (Rene vessel) unloading data at P values of 30, 50, and 85 MPa are presented in Figure 5a, where they are compared to the hydrostatic bulk moduli obtained in our hydrostatic plus deviatoric experiments. For given P and similar φ_0 values, K values obtained in the purely hydrostatic (Rene) experiments are similar to those obtained in the hydrostatic unloading stages of combined hydrostatic plus deviatoric experiments, within the error of 10% determined for the former (Rene) set of K (Figure 5a). Note that the similar P versus $\Delta\varphi_t$, $\Delta\varphi_i$, and K behaviors obtained using the pore volume data of combined hydrostatic plus deviatoric tests versus those determined using the bulk volume data of the hydrostatic (Rene) tests suggests that our initial assumption of roughly equal bulk and pore volume responses (see section 3.4.2) was a good approximation.

4.3. Sample-Scale Observations and Microstructural Data

4.3.1. Sample Scale

Posttest, visual inspection of samples tested in combined hydrostatic plus deviatoric stress cycling experiments revealed a single shear fracture in each of the low porosity samples that showed Stage 3d (i.e., dilatant) behavior at effective confining pressures P_c^{eff} of 5, 20, and 40 MPa (samples z20a, z20d, and z20c, respectively). In these samples, the angle of the fracture plane to the core axis (i.e., the main compression direction) increased from 25° to 40° with increasing test P_c^{eff} . The low porosity sample z20b, which showed Stage 3c behavior during deviatoric stress cycling at $P_c^{\text{eff}} = 80$ MPa (Figure 4a) and the intermediate porosity sample z24d, yielding Stage 3d behavior during deviatoric stress cycling at $P_c^{\text{eff}} = 20$ MPa (Figure 4b), revealed multiple, conjugate fractures, located within 20 mm of one sample end. These fractures were orientated at an angle of about $70^\circ \pm 10^\circ$ to the core axis. No macroscopically visible deformation features were observed in any of the remaining experiments, deviatoric, or hydrostatic.

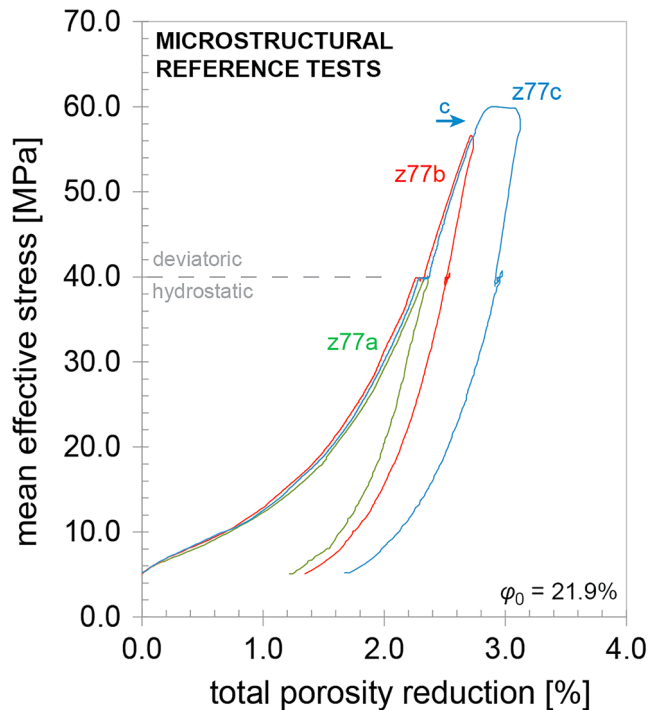


Figure 7. Plot showing mean effective stress (P) versus total porosity reduction ($\Delta\phi_t$) data obtained in our hydrostatic plus deviatoric microstructural reference tests. Samples z77a, z77b, and z77c were deformed up to parts of the P - $\Delta\phi_t$ curve corresponding approximately to the end of Stages 1, 2, and 3c, respectively, as defined in Figure 2. These samples were used to investigate the grain-scale mechanisms accommodating inelastic compaction in each of these stages.

initial porosity of 21.9% (z77a–z77c). The experiments consisted of monotonic, hydrostatic, and then deviatoric loading and unloading only (no cycling). The mean effective stress versus total porosity reduction data obtained in these tests are presented in Figure 7. The data show closely reproducible uploading behavior. All samples showed concave-up P - $\Delta\phi_t$ behavior up to $P \approx 35$ MPa and $\Delta\phi_t \approx 2.0\%$. Samples z77b and z77c showed near-linear behavior beyond this, up to $P \approx 58$ MPa ($Q = 54$ MPa) and $\Delta\phi_t \approx 2.8\%$, at which point z77b was unloaded. Further loading of sample z77c produced a short interval of strain-hardening at decreasing rate (Stage 3c), leading to a broad peak in mean effective stress of $P = 59.7$ MPa ($Q_{\text{peak}} = 59.1$ MPa), at $\Delta\phi_t = 2.9\%$, after which minor strain softening occurred (<1 MPa). After unloading to the reference mean effective stress of 5 MPa, samples z77a, z77b, and z77c showed final inelastic porosity reductions ($\Delta\phi_{i,\text{fin}}$) of 1.24%, 1.35%, and 1.68%, respectively. Overall, the P - $\Delta\phi_t$ behavior shown was closely similar to that obtained in the stress cycled, hydrostatic plus deviatoric experiments performed at the same conditions on sample z24c with similar initial porosity ($\phi_0 = 21.5\%$; Figure 4b).

5.2. Microstructural Data

The intragranular crack densities determined along the plug axis of reference test samples z77a–z77c ($\phi_0 = 21.9\%$) and undeformed counterpart sample z77 are plotted in Figure 8. The undeformed sample shows a mean crack density ($\bar{\rho}_{cr}$) of 12.8 mm^{-2} (Figure 8a). The distribution of crack densities along the length of the sample is roughly uniform and is characterized by a SD of 6.6 mm^{-2} from the mean. In samples z77a, compressed hydrostatically to $P_c^{\text{eff}} = 0$ MPa, and z77b, which was additionally loaded deviatorically to $Q = 50$ MPa, the mean crack densities are slightly higher, specifically 14.2 and 17.7 mm^{-2} , respectively. In sample z77a, the crack density distribution is still approximately uniform (SD = 7.7 mm^{-2}). In sample z77b, the crack density distribution remains uniform in the bulk of the sample, but higher values are locally seen near the top and bottom of this sample, reaching 50 mm^{-2} . By contrast, Sample z77c, deviatorically compressed at $P_c^{\text{eff}} = 40$ MPa beyond the peak stress ($P = 59.7$ MPa, $Q_{\text{peak}} = 59.1$ MPa), shows a mean crack density of 55.3 mm^{-2} . Moreover, the crack density distribution is highly heterogeneous (SD = 29.1), locally

4.3.2. Microstructure

Mean crack density data obtained as described in Section 3.5 from BSE images of our deformed samples and of their undeformed counterparts are shown in Table 1. A detailed description of the individual distributions of intragranular crack densities across the length of each sample analyzed is given in the supporting information S4. In brief, all undeformed samples showed a roughly uniform crack density distribution, with low mean crack density values ($\bar{\rho}_{cr}$) in the range of 5 to 12 mm^{-2} (Table 1). All deformed samples analyzed showed higher $\bar{\rho}_{cr}$ than seen in their undeformed counterparts, ranging from 10 to 73 mm^{-2} where values increased with increasing testing effective confining pressure (Table 1). The highest mean crack density was seen in the hydrostatically deformed sample z24e, revealing a roughly uniform crack density distribution. In samples deformed in our hydrostatic plus deviatoric tests, the increase in intragranular cracks was highly heterogeneous, where most cracks were seen along in 1 to 10 mm wide sections along the profile lines. In viewing the stitched micrographs at multiple scales, one can see that these high crack densities reflect intersection of the profile line with diffuse bands of high crack density (see supporting information S4). Where macroscopic features were observed, high crack density bands reflected the intersection of these inclined features (as was the case for z20c and z24d). Where no macroscopically visible deformation feature was present, high crack density bands were often oriented subperpendicular ($\pm 20^\circ$) to the main compression direction.

5. Microstructural Reference Test Results

5.1. Mechanical Data

It will be recalled that these experiments consisted of combined hydrostatic plus deviatoric tests performed on samples with an intermediate

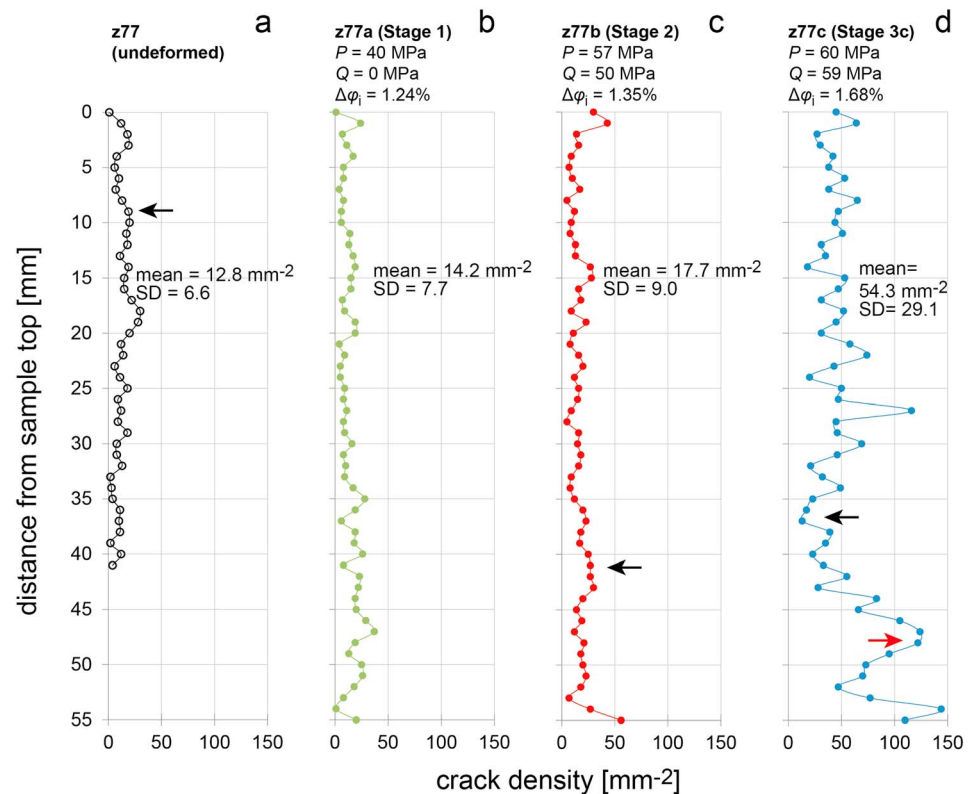


Figure 8. Plots showing the intragranular crack density (cracks per mm^2) distribution along the length of each sample ($\varphi_0 = 21.9\%$) deformed in microstructural reference tests (Figure 7), and of their undeformed counterpart. Mean crack densities, the standard deviation of the crack density distribution, and the final inelastic porosity reductions ($\Delta\varphi_{i,\text{fin}}$) measured at the end of each test are indicated. Arrows indicate the sample depths of the micrographs shown in Figure 9. (a) Undeformed sample z77, showing a roughly uniform crack density distribution. (b) Sample z77a, deformed into Stage 1. (c) Sample z77b, deformed into Stage 2. (d) Sample z77c, deformed into Stage 3c, and beyond failure. Note the markedly increased, heterogeneously distributed crack densities in this sample.

showing values as high as $70\text{--}150\text{ mm}^{-2}$, notably at 27 and 44–51 mm from the sample top and in the bottom 3 mm of the sample (Figure 8c). Viewing the micrographs at multiple scales (see supporting information) showed that these high crack densities reflect intersection with 2- to 10-mm wide, diffuse bands of high crack density, which are oriented subperpendicular ($\pm 20^\circ$) to the main compression direction.

To illustrate the general microstructural character of our microstructural reference test samples, representative BSE micrographs were selected from the locations indicated in Figure 8 (arrows) and are presented in Figure 9. The undeformed sample (Figure 9a) is composed of predominantly quartz grains ($\sim 75\text{ vol}\%$), with lesser amounts of feldspar ($\sim 20\text{ vol}\%$), and clays ($\sim 5\text{ vol}\%$). The latter two are clearly highlighted in an Al element map obtained using electron dispersive X-ray spectrometry (Figure 9b). Quartz and feldspar grains are typically $100\text{--}200\text{ }\mu\text{m}$ in size, subrounded, slightly elongated, and frequently oriented with their long axes perpendicular to the sample/core axis (= parallel to sedimentary lamination). Clay films coating the pore walls are often relatively thick ($5\text{--}20\text{ }\mu\text{m}$), while thinner clay films ($1\text{--}5\text{ }\mu\text{m}$) are found within grain contacts (Figure 9b). In both undeformed and deformed samples, intragranular cracks typically emanate from the periphery of grain-to-grain contacts (yellow arrows, in Figure 9) or from within grain contacts (white arrows), where they are often found at small grain contact asperities ($<10\text{ }\mu\text{m}$) or at intergranular pores (Figure 9d). In parts of the deformed samples where the intragranular crack density is relatively low ($<30\text{ mm}^{-2}$; see black arrows, in Figure 8), the corresponding microstructure (Figures 9c–9e) is essentially indistinguishable from that of the undeformed counterpart (Figure 9a). By contrast, in the high crack density regions seen in deformed sample z77c (e.g., red arrow, Figure 8d), intragranular and transgranular cracks are ubiquitous, being associated with pervasive grain crushing in triangular regions at quartz/feldspar grain contacts and in transgranular zones spanning individual and multiple grains (red arrows, Figure 9f).

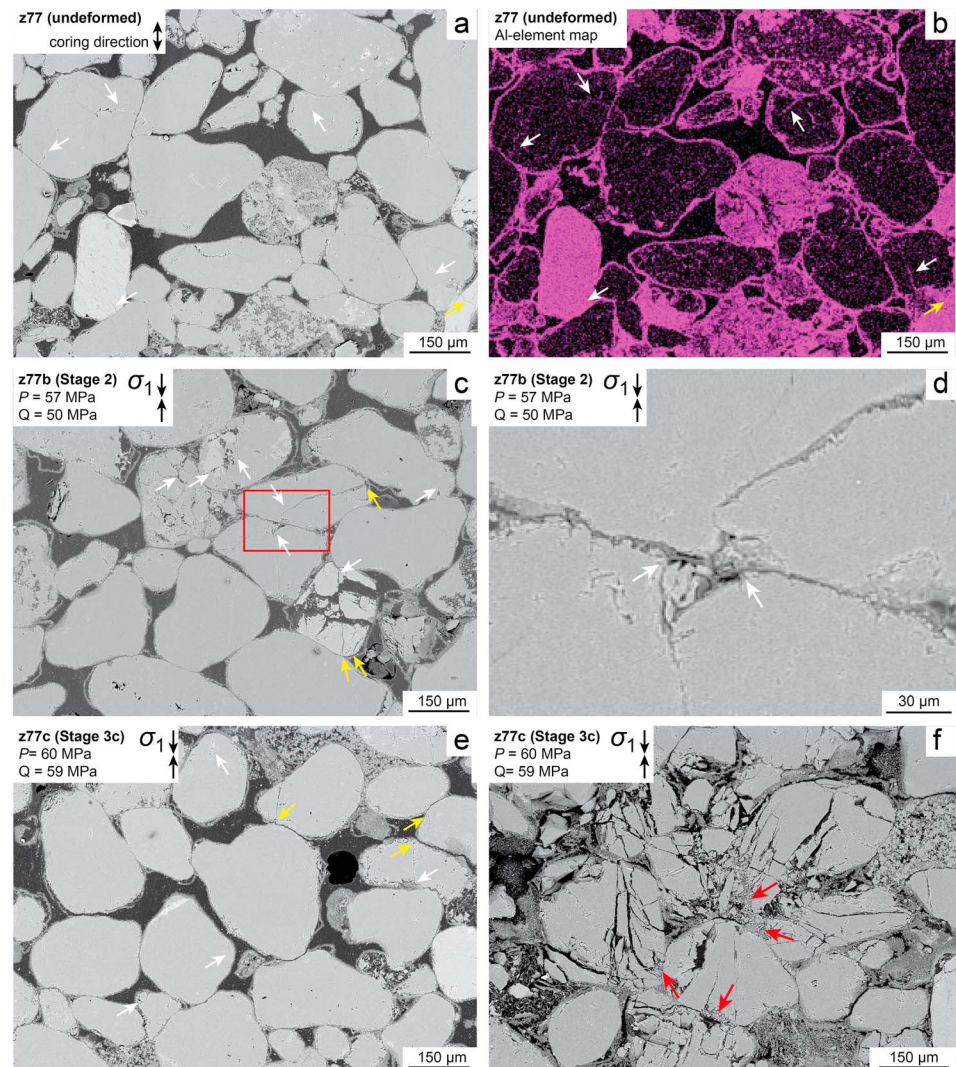


Figure 9. Backscatter electron micrographs recovered from samples ($\phi_0 = 21.9\%$), deformed in our microstructural reference tests (Figure 7) and from their undeformed counterpart. The locations of these micrographs are indicated with arrows in Figure 8. White and yellow arrows indicate intragranular cracks emanating, respectively, from within grain contacts or from the peripheries of grain contacts. (a) The undeformed sample z77 shows few intragranular cracks. (b) Same view as in (a), showing regions of high aluminum content, highlighting feldspar and clay films coating the pore walls and grain contacts. (c) Sample z77b, compressed into Stage 2, showing a microstructure similar to that of the undeformed sample. (d) Close-up from (c), showing a thin clay film present within a rough grain contact. Intragranular cracks emanate from a pore present within this grain contact. (e) Micrograph obtained from a low crack density region (black arrow in Figure 8d) of sample z77c deformed into Stage 3c, showing a very similar microstructure to its undeformed counterpart (a). (f) Micrograph obtained from a high crack density region (red arrow in Figure 8d) of the same sample z77c, showing pervasive grain crushing (red arrows).

6. Discussion

The mean effective stress (P) versus total porosity reduction ($\Delta\phi_t$) and inelastic porosity reduction ($\Delta\phi_i$) data presented here for Slochteren sandstone show a clear transition from initial, nonlinear, concave-up behavior (Stage 1; compare Figures 3, 4, and 6 with Figure 2), to subsequent near-linear behavior (Stage 2) and final, nonlinear, dilatant (Stage 3d), or compactant behavior (Stage 3c). Both elastic and inelastic deformation contributed significantly to each of these stages, including in the near-linear Stage 2 (Figures 3, 4, and 6), which is often assumed to reflect poroelastic deformation only (see Introduction). During Stage 2, the total hardening rates (i.e., $dP/d\Delta\phi_t$) and inelastic hardening rates (i.e., $dP/d\Delta\phi_i$) were both found similar during deviatoric and hydrostatic uploading, indicating isotropic behavior. Total hardening rates constituted a

near-constant 8.3 ± 0.5 GPa in low porosity sandstone ($\varphi_0 = 13.4\%–13.9\%$), 5.7 ± 0.4 GPa at intermediate porosities ($\varphi_0 = 21.4\%–21.5\%$), and 4.1 ± 0.5 GPa in high porosity samples ($\varphi_0 = 25.6\%–26.4\%$). Corresponding inelastic hardening rates (i.e., $dP/d\Delta\varphi_i$) were 27.8 ± 1.2 GPa (low φ_0), 16.7 ± 0.7 GPa (intermediate φ_0), and 9.8 ± 0.5 GPa (high φ_0). Thus, during Stage 2, approximately 30% to 50% of the total porosity reduction was inelastic. At higher stresses, that is, in Stages 3d and 3c, a similar inelastic contribution was demonstrated, with final total porosity reductions ($\Delta\varphi_i$)_{fin} ranging from -0.4% (dilatant; at $P_c^{\text{eff}} = 5$ MPa) to 7.4% (compactive), to which inelastic deformation contributed -0.1% to 3.2% in absolute terms (Table 1). Crucially, we demonstrated that the stress cycling method employed to quantify the reported $P-\Delta\varphi_i$ and $Q-\varepsilon_i$ behavior did not impact the overall stress-strain behavior through effects such as damage accumulation (Figure 3). Bulk and Young's moduli characterizing the elastic component of deformation were shown to increase with increasing mean effective stress, and with decreasing initial porosity (Figure 5). After Stage 1 and 2 deformations, micrographs showed a small increase in intragranular crack density ($\bar{\rho}_{cr} = 14.1$ and 17.2 mm⁻²) with respect to the undeformed counterpart samples ($\bar{\rho}_{cr} = 12.8$ mm⁻²). By contrast, after Stage 3d or Stage 3c deformations, intragranular crack densities were generally higher ($\bar{\rho}_{cr} = 10$ to 72 mm⁻²; Table 1).

6.1. Elastic Behavior of the Slochteren Sandstone

The present data on the truly elastic behavior of our samples yielded bulk moduli in the range 1 to 11 GPa and Young's moduli varying from 3 to 22 GPa. Both were found to increase with increasing mean effective stress (P) and with decreasing initial sample porosity (φ_0 ; Figure 5). Stiffening of elastic moduli with increasing mean effective stress and decreasing initial porosity is well known in sandstones (Blöcher et al., 2014; Chang et al., 2006; Fortin et al., 2005; Heap et al., 2010; Ingraham et al., 2017). These effects occur because the (average) grain contact area and (quasi-Hertzian) contact stiffness increases with decreasing initial porosity and with increasing grain contact compression (Digby, 1981; Walton, 1987).

At low mean effective stresses (≤ 30 MPa), corresponding to Stage 3d behavior in samples deviatorically tested at $P_c^{\text{eff}} = 5$ MPa and to Stage 1 behavior in all other samples, K values obtained during (Stage 1) hydrostatic unloading were more compliant than those seen during (Stage 3d) deviatoric unloading at $P_c^{\text{eff}} = 5$ and 20 MPa, suggesting anisotropic elastic behavior. By contrast, at P values of 50 and 85 MPa, corresponding to the near-linear Stage 2 during both deviatoric and hydrostatic unloading, K was found to be similar in both deviatoric and hydrostatic unloading. This suggests that during Stage 2, the elastic behavior was isotropic. In line with previous work (David et al., 2012; Walsh, 1965), we suggest that the anisotropic versus isotropic behaviors were controlled by the elastic closure and opening of intragranular cracks and possibly dilated grain boundaries during loading and unloading, respectively. In part, intragranular cracks are already present in the microstructure (Figure 8a). In addition, low confinement ($P_c^{\text{eff}} = 5$ MPa), deviatoric Stage 3d compression was shown to lead to an increase in such cracks (see section 4.3.2) likely increasing the anisotropy. By contrast, during progressive Stage 1 hydrostatic compression, virtually no new intragranular cracks were formed (Figure 8b), while preexisting cracks are progressively closed and are fully closed at the onset of the near-linear Stage 2.

6.2. Inelastic Deformation Mechanisms in the Present Experiments

As noted in the introduction, the mechanisms accommodating inelastic deformation of sandstone under low temperature, laboratory conditions ($T < 150$ °C) and relatively rapid strain or loading rates ($\dot{\varepsilon}_t \sim 10^{-5}$ s⁻¹; $\dot{P} \sim 0.1$ MPa s⁻¹) have often been reported to include intragranular cracking, intergranular cracking, and intergranular shear displacements. In addition, during each of the three deformation stages seen in previous P versus $\Delta\varphi_t$ data for sandstones (Figure 2), these inelastic mechanisms are thought to partition differently (Bernabe et al., 1994; Menéndez et al., 1996; Renard et al., 2017; Wu et al., 2000). In line with this, our microstructural reference samples z77a–z77c, deformed to the end of Stages 1 (z77a), 2 (z77b), and 3c (z77c; Figure 7) showed mean intragranular crack densities per unit final inelastic porosity reduction of 11.4, 13.1, and 32.3 mm⁻²/%, respectively. To investigate the role played by intragranular cracking in accommodating inelastic porosity reduction more specifically for each individual deformation stage, we assume that the initial microstructures of our three deformed reference samples, z77a–z77c were equivalent prior to testing and hence to that of the undeformed sample (z77). We further assume that the reproducible $P-\Delta\varphi_t$ behavior seen during testing (Figure 7) implies similar microstructural evolution. The role played by intragranular cracking per unit inelastic porosity reduction in each stage can then be quantified from the

changes in mean crack density and final inelastic porosity reduction measured in progressing from the undeformed sample, to sample z77a (end Stage 1), to sample z77b (end Stage 2), and to sample z77c (end Stage 3c). The resulting stage-specific changes in mean crack density per unit porosity reduction were 1.1, 32.4, and 110.7 mm⁻²/%, respectively, while the corresponding strain-normalized standard deviations were 6.2, 6.7, and 17.3 mm⁻²/%, respectively. These results suggest that the role played by intragranular cracking in achieving inelastic porosity reduction is negligible during Stage 1, small during Stage 2, and much larger during Stage 3c (cf. Menéndez et al., 1996; Wu et al., 2000).

As indicated earlier, the initial, compliant, and nonlinear P - $\Delta\phi_i$ behavior defining Stage 1 is commonly attributed to the progressive elastic/inelastic closure of preexisting, intergranular and/or intragranular cracks (David et al., 2012; Walsh, 1965), which is consistent with the lack of any increase in crack density seen after Stage 1 deformation only (Figure 8b). Beyond Stage 1 and into Stage 2 at $P > 35$ MPa, near linear yet partially inelastic (30%–50%) P - $\Delta\phi_i$ behavior followed, suggesting a change in both elastic and inelastic deformation mechanisms. Interestingly, this mean effective stress of 35 MPa is similar to the mean effective stresses of 39 MPa, measured in the Slochteren sandstone reservoir in Zeerijp at the time of core extraction (van Eijs, 2015). This may suggest that intergranular and/or intragranular cracks were introduced to our samples as “core damage” during release of the in situ stresses supported by the sample during core extraction (Holt et al., 2000; Santarelli & Dusseault, 1991). It is anticipated, then, that while exploring mean effective stresses exceeding those prevalent in the reservoir (i.e., $P > 39$ MPa), such initial damage effects are largely removed and the inelastic strains measured from this point onward are newly induced.

During Stage 2, the importance of intragranular cracking per unit inelastic porosity reduction was larger, but still much smaller than that seen during Stage 3c. Therefore, for the bulk of Stage 2, we speculate that intergranular normal and/or shear displacements likely accommodated most of the inelastic deformation, beyond the “damage closure” effects of Stage 1. Normal grain boundary displacements could potentially occur by internal grain contact asperity breakage or through the squeezing and/or dewatering of intergranular clay films at contacts under concentrated normal stress (e.g., Figures 9b and 9d). We note, though, that microstructural evidence for such intergranular normal and shear displacements or the accommodating mechanism is still lacking and requires further investigation.

Aside from minor increases in intragranular crack density seen at the ends of sample z77b, deformed into Stage 2, no evidence for localization was observed (Figures 8b and 8c). By contrast, all of the microstructurally investigated samples, deformed into the nonlinear Stages 3d and 3c of the P - $\Delta\phi_i$ curve showed a marked increase in intragranular crack density (Figure 9f) within localized bands (see supporting information S4). Within these bands, pervasive grain and grain contact crushing was seen, especially in samples deviatorically tested at $P_c^{\text{eff}} \geq 40$ MPa (Figure 9f). In addition, all low porosity samples subjected to deviatoric loading into Stages 3d and 3c, as well as intermediate porosity sample z24d tested in deviatoric compression at $P_c^{\text{eff}} = 20$ MPa showed macroscopically visible, localized shear bands. These results are in good agreement with previous experiments on sandstone, which have demonstrated that Stage 3d/3c deformation leads to a significant, localized increase in acoustic emissions (DiGiovanni et al., 2007; Fortin et al., 2006), intragranular cracks (Baud et al., 2004; Tembe et al., 2008), and porosity change (Fortin et al., 2005; Renard et al., 2017).

6.3. Effects of Initial Porosity and Inelastic Porosity Reduction on Strain Hardening

Here we analyze the effect of initial porosity and inelastic porosity reduction on the hardening behavior shown by our samples, for the full range of stress conditions explored. The results form the basis needed for assessing to what extent our data can be described by a granular medium plasticity model in which the P - $\Delta\phi_i$ or Q - ε_i behavior is solely dependent on initial porosity and inelastic porosity reduction.

To investigate the sensitivity of the hardening behavior shown by our samples to initial porosity and to inelastic porosity reduction, we contour fixed values of inelastic porosity reduction developed during all stages of strain hardening behavior in differential stress (Q) versus mean effective stress (P) space for each set of samples with similar initial porosity (within 0.8%; Figure 10; cf. Karner et al., 2005; Wong et al., 1992). Compaction occurring during strain-neutral or strain-softening behavior is not contoured. We assume that the values of Q , P , and $\Delta\phi_i$ measured after any two consecutive stress cycles of the same experiment can each be interpolated linearly, to obtain the stress conditions matching fixed 0.1% increments in $\Delta\phi_i$. For reference, the maximum stress states imposed in individual stress cycles are indicated in Figure 10 with black dots. Peak stress conditions beyond

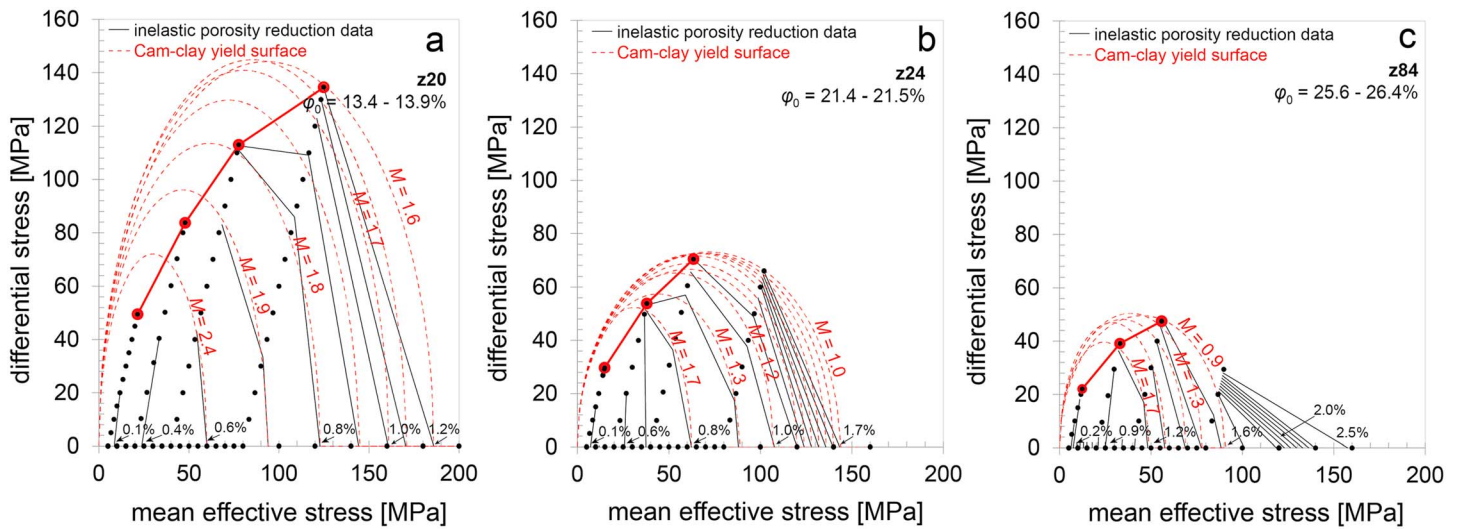


Figure 10. Plots showing the differential stress (Q) versus mean effective stress (P) conditions required for strain softening (i.e., failure—solid red lines) and to induce the indicated values of inelastic porosity reduction (black contour lines), in our samples with (a) low (ϕ_0 = of 13.4%–13.9%), (b) intermediate (ϕ_0 = of 21.4%–21.5%), and (c) high initial porosities (ϕ_0 = of 25.6%–26.4%). Only porosity reductions accompanied by strain hardening (positive slopes of P – $\Delta\phi_i$ curves in Figures 4 and 6) are contoured. Black dots represent the maximum stress conditions imposed in each stress cycle. The differential stresses delineated by inelastic porosity reduction contours show a direct P dependence at low P , transitioning into an inverse P dependence at higher P . Where an inverse P dependence is observed, these data are compared to modified Cam-clay yield envelopes (dashed red ellipses; see section 6.4.1). However, for the highest inelastic porosity reductions ($\geq 1.7\%$) seen in our high porosity samples, no adequate fit could be achieved. The M factors controlling the shape of the yield envelope generally decrease with increasing inelastic porosity reduction.

which strain-softening behavior was observed (i.e., Q_{peak} in Table 1 and the corresponding P) are encircled in red and are used to delineate the stress conditions required for failure in samples with low ($\phi_0 = 13.4\%$ – 13.9%), intermediate ($\phi_0 = 21.4\%$ – 21.5%), and high initial porosity ($\phi_0 = 25.6\%$ – 26.4%).

The red failure lines plotted in Figure 10 for samples with low, intermediate, and high initial porosities show a positive, slightly downward curved slope in Q versus P space, with average slopes of about 1.1, 0.8, and 0.6, respectively. These slopes, their porosity dependence, and the dilatant failure modes observed at low P (i.e., Stage 3d; Figures 4a–4c) are qualitatively consistent with typical, Mohr-Coulomb shear behavior (e.g., Paterson & Wong, 2005), involving intergranular cracking plus frictional, intergranular slip (Guéguen & Fortin, 2013). The inelastic porosity reduction contours (black lines in Figure 10) are orientated at high angles to the red failure lines. From the orientations of these contour lines and from their spacing, three different types of inelastic deformation behavior can be distinguished, as described below. These correspond to the inelastic porosity reduction values associated with Stage 1 (see Figure 2), near-linear Stage 2, and final nonlinear Stage 3c behavior (Figures 4a–4c).

During Stage 1 (P up to 35 MPa), relatively large inelastic porosity reductions were measured in both hydrostatic and deviatoric compression, with $\Delta\phi_i$ up to 0.6% in low porosity samples ($\phi_0 = 13.4\%$ – 13.9%), $\Delta\phi_i$ up to 0.8% for intermediate porosities ($\phi_0 = 21.4\%$ – 21.5%), and $\Delta\phi_i$ up to 1.2% in the high porosity sandstones ($\phi_0 = 25.6\%$ – 26.4%). For these values of $\Delta\phi_i$, inelastic porosity reduction contours (black lines, Figure 10) are closely spaced and are characterized by steep positive to near-vertical slopes. Hence, at these conditions, inelastic compaction behavior is highly compliant, strongly dependent on the mean effective stress and almost independent of differential stress. This implies that the deformation mechanism inferred to control Stage 1 inelastic deformation, that is, intergranular or interparticle closure of preexisting damage is predominantly controlled by P not by Q (see also Karner et al., 2005).

During Stage 2, inelastic porosity reductions ranged from approximately 0.6% to 1.0% ($\phi_0 = 13.4\%$ – 13.9% ; see Table 1), 0.8% to 1.1% ($\phi_0 = 21.4\%$ – 21.5%), and 1.2% to 1.7% ($\phi_0 = 25.6\%$ – 26.4%). For these values of $\Delta\phi_i$, the spacing between inelastic porosity reduction contours is wider. At the onset of Stage 2, the differential stresses delineated by individual contours show a minor inverse dependence on P . With increasing Q and P , this inverse dependence increases (i.e., the slope of contour lines becomes less negative), until the shear failure line, or Stage 3c is reached. This suggests a transition in behavior of the mechanisms suggested to control inelastic

compaction during Stage 2 (i.e., grain boundary asperity breakage and/or consolidation and shear of intergranular clays, with a smaller role played by intragranular cracking—see previous section) from being initially primarily P sensitive, to becoming increasingly more sensitive to Q toward the later stages of Stage 2 and into Stage 3c.

Stage 3c hardening behavior was seen at $\Delta\phi_i > 1.0\%$ (low porosity) $> 1.1\%$ (intermediate porosity) and $> 1.7\%$ (high porosity). Here all samples and particularly the intermediate and high porosity ones ($\phi_0 \geq 21.4\%$) showed Q - and P -sensitive contour lines, where a marked decrease in their spacing implies increased inelastic compaction rates. Such differential stress- or shear-enhanced compaction behavior is well known to occur during Stage 3c (Baud et al., 2006; Curran & Carroll, 1979; Tembe et al., 2008; Wong et al., 1997). This behavior is thought to be controlled by intragranular cracking, which is favored upon tangential loading of grain contacts (Shah & Wong, 1997). It appears, then, that compaction during the initial stages of Stage 2 is accommodated by predominantly Q insensitive, intergranular processes, where the progressive decrease in slope of Stage 2 contour lines (increasing Q -sensitivity) reflects an increasing role played by intragranular cracking, becoming dominant in Stage 3c.

6.4. Comparison With Plasticity Theory

6.4.1. Modified Cam-Clay Yield Envelope

We now make use of the data plotted in Figure 10 to explore to what extent the present stress versus inelastic strain data can be described using the general plasticity theory for granular media outlined by Muir Wood (1991, Chapter 4). In principle, this theory provides a description for the stress versus inelastic strain behavior for yield envelopes of any shape in P - Q space. Here we use the modified Cam-clay yield function, because of its previous use in geomechanical modelling of upper crustal hydrocarbon reservoirs (Chan et al., 2004; Crawford et al., 2011) and in more generic studies of inelastic sandstone deformation (Schultz & Siddharthan, 2005; Skurtveit et al., 2013). In the modified Cam-clay formulation, the stress conditions required for yield are described in differential stress ($Q = [\sigma_1 - \sigma_3]$) versus mean effective stress ($P = [\sigma_1 + 2\sigma_3]/3 - P_p$) space, by the following elliptical function:

$$f(Q, P, \sigma^*) = Q^2 - M^2 P (\sigma^* - P) = 0 \quad (1)$$

Here σ^* is the hydrostatic mean effective stress required for the onset of inelastic deformation, and M is the slope of the critical state line, along which inelastic axial compression occurs at zero inelastic volume change. The factors σ^* and M control the size and height-over-width ratio (i.e., the ellipticity) of the yield envelope, respectively. Most models for inelastic deformation of granular media utilizing plasticity theory, such as the modified Cam-clay model (Muir Wood, 1991), the critical state model (Schofield & Wroth, 1968), and the cap-model (DiMaggio & Sandler, 1971) assume that hardening occurs with inelastic porosity reduction only and with no effect of inelastic axial strain or shear strain. To test to what extent this assumption applies to our experiments, we directly compare the modified Cam-clay yield surfaces described by equation (1) (i.e., the stress conditions required to achieve a given value of compaction), to the inelastic porosity reduction contours outlined in Figure 10. In doing so, the σ^* value used to construct a yield surface using equation (1) is given by the mean effective stress required to induce the corresponding value of inelastic porosity reduction during our hydrostatic tests. Since inelastic porosity reduction was observed from the onset of compression (Figures 3, 4, and 6), this means that the initial value of σ^* is equal to the mean effective stress of 5 MPa imposed at the start of each experiment. The shape factor M was varied for each yield envelope, until a best fit to the corresponding contour line was achieved, based on visual inspection. For each yield envelope fitted in this way, the uncertainty in M was estimated by exploring the M values for which the yield envelope fitted at least two data points defining the corresponding contour. The uncertainty in M was found to be ± 0.1 (i.e., $\pm 5\%$ – 15%). Note, though, that each of these yield envelopes is typically constrained by only three data points, meaning that additional uncertainty in M will exist due to sample variation. Ideally, more experimental data would be available for samples with the same porosity values, that is, from the same depth intervals used here. In the present study, the number of samples per core interval was limited by the diameter of the core (~ 10 cm). Alternatively, more detailed delineation of inelastic porosity reduction contours could be attempted using the method outlined by Tembe et al. (2007), in which the confining pressure and axial stress imposed in a triaxial test are manipulated simultaneously so as to maintain constant pore volume.

Returning to the comparison of our data with the Cam-clay model, for the low inelastic porosity reductions of $\Delta\phi_i < 0.6\%$ ($\phi_0 = 13.4\%$ – 13.9%), $\Delta\phi_i < 0.8\%$ ($\phi_0 = 21.4\%$ – 21.5%), and $\Delta\phi_i < 1.2\%$ ($\phi_0 = 25.6\%$ – 26.4%),

corresponding to Stage 1 deformation, the fit between inelastic porosity reduction lines and elliptical Cam-clay yield surface was poor. However, at greater inelastic porosity reductions of up to 1.2% ($\varphi_0 = 13.4\%$ – 13.9%), 1.7% ($\varphi_0 = 21.4\%$ – 21.5%), and 1.6% ($\varphi_0 = 25.6\%$ – 26.4%), corresponding to Stages 2 and 3c deformation (Figures 4a–4c), the stress conditions outlined by inelastic porosity contours were reasonably well described by the Cam-clay yield surfaces shown in Figure 10 (i.e., within a difference in Q or P of 5 MPa). The shape factor M used to construct the envelopes shown for samples deformed in Stages 2 and 3c ranged from 2.4 to 0.9 and decreased with increasing inelastic porosity reduction. The highest M values were obtained for our samples with the lowest initial porosity during Stage 2 ($\varphi_0 = 13.4\%$ – 13.9% ; Figure 10a). Similar trends have been seen in previous work on bassanite, showing a decreasing height-over-width ratio of the yield envelope with increasing inelastic compaction (Bedford et al., 2018). For our high porosity samples ($\varphi_0 = 25.6\%$ – 26.4%), the Stage 3c behavior ($\Delta\varphi_i > 1.7\%$) could not be fitted with elliptical yield envelopes, without having these envelopes cross the envelopes corresponding to the lower inelastic porosity reductions of Stage 2 (Figure 10c). Rather, for these highly porous samples and the Stage 3c porosity reductions, a linear end-cap, rather than an elliptical one may be more appropriate, such as proposed by Guéguen and Fortin (2013).

6.4.2. Normality Condition

The Muir Wood plasticity theory predicts that during yielding of isotropic, granular materials, each increment of inelastic strain develops normal to the yield surface, that is, these materials obey the normality or associative flow condition (Muir Wood, 1991; see also Desai & Siriwardane, 1984). If the normality condition is not satisfied, more complex, nonassociative models are required (e.g., Issen & Rudnicki, 2000; Rudnicki & Rice, 1975). Here we test whether the condition holds for the yield surfaces drawn in Figure 10. In P – Q space, the normality condition implies that the ratio between the increments of inelastic volumetric strain ($d\varepsilon_{v,i} = d\varepsilon_i + 2d\varepsilon_{3,i}$) and inelastic shear strain ($dy_i = 2/3[d\varepsilon_i - d\varepsilon_{3,i}]$) developing upon an incremental increase of the mean effective stress (dP) and/or differential stress (dQ) satisfies the relations (Muir Wood, 1991):

$$\frac{d\varepsilon_{v,i}}{dy_i} = \frac{\delta f / \delta P}{\delta f / \delta Q} = \frac{M^2 - \left(\frac{Q}{P}\right)^2}{2 \frac{Q}{P}} \quad (2)$$

Noting that $\varepsilon_{v,i} \approx \Delta\varphi_i$ (see section 3.4.2), equation (2) can be rewritten as the ratio between the inelastic porosity reduction and the inelastic axial strain:

$$\frac{d\Delta\varphi_i}{d\varepsilon_i} = \frac{3 \left(M^2 - \left(\frac{Q}{P} \right)^2 \right)}{6 \frac{Q}{P} + M^2 - \left(\frac{Q}{P} \right)^2} \quad (3)$$

Inserting the M values obtained for each yield envelope shown in Figure 10 into equation (3), we predicted the $\frac{d\Delta\varphi_i}{d\varepsilon_i}$ versus P behavior implied by these envelopes if the normality condition applies. The predicted curves are shown in Figure 11, where they are compared to experimental $\frac{\Delta(\Delta\varphi_i)}{\Delta\varepsilon_i}$ versus P data, measured during the deviatoric stages of our hydrostatic plus deviatoric experiments at the relevant initial porosity and inelastic porosity reduction values (red and blue symbols). Red and blue symbols indicate that the corresponding data points were obtained within, respectively, the near linear (Stage 2—red) and the subsequent nonlinear (Stage 3c—blue) portions of the P versus $\Delta\varphi_t$ curves shown in Figure 4. For reference, we include the P – $\Delta\varphi_i$ data obtained in the purely hydrostatic testing in the Rene vessel (Figure 6), by assuming isotropic, inelastic compaction behavior, so that $\Delta\varepsilon_i = \Delta\varepsilon_{2,i} = \Delta\varepsilon_{3,i}$, implying $\Delta(\Delta\varphi_i) \approx 3\Delta\varepsilon_i$. For these samples, $\frac{\Delta(\Delta\varphi_i)}{\Delta\varepsilon_i}$ is accordingly assumed to be equal to 3 (grey symbols).

Figure 11 shows that for the same values of mean effective stress, initial porosity, and inelastic porosity reduction, the $\frac{\Delta(\Delta\varphi_i)}{\Delta\varepsilon_i}$ values obtained during deviatoric stress cycling in Stage 2 (red) are similar to those predicted assuming normality. Hence, during the near linear, Stage 2 part of the P – $\Delta\varphi_t$ curve, the normality condition is satisfied. This, combined with (a) the similar hardening behavior shown during Stage 2 hydrostatic and deviatoric compression (Figures 4a–4c) and (b) the absence of significant localization shown by the intragranular crack density profile measured after Stage 2 deformation (Figure 8c), implies that inelastic deformation in Slochteren sandstone behaves isotropically during Stage 2. Furthermore, since the yield envelopes in Figure 10 were fitted to inelastic porosity reduction contours (thus ignoring any influence of inelastic axial strain) Stage 2 hardening must be predominantly controlled by inelastic porosity reduction, with a negligible influence of inelastic axial strain.

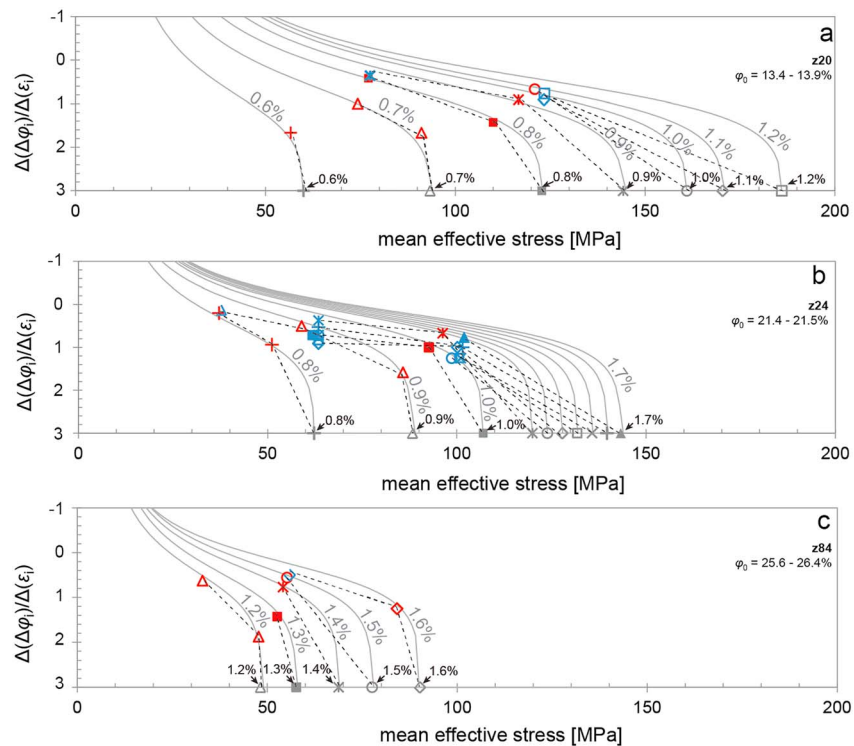


Figure 11. Plots showing the ratio of changes in inelastic porosity reduction and inelastic axial strain $\Delta(\Delta\varphi_i)/\Delta(\varepsilon_i)$ versus mean effective stress data (P), obtained for the contoured values of inelastic porosity reduction measured in samples with (a) low ($\varphi_0 =$ of 13.4%–13.9%), (b) intermediate ($\varphi_0 =$ of 21.4%–21.5%), and (c) high initial porosities ($\varphi_0 =$ of 25.6%–26.4%). Only the data that were adequately fitted to Cam-clay yield surfaces in Figure 10 are shown. Red and blue symbols indicate data obtained during deviatoric stress cycling from the near-linear (Stage 2) and nonlinear, compactant (Stage 3c) parts of the present P – $\Delta\varphi_t$ curves (Figure 4). The P – $\Delta\varphi_i$ data obtained in our hydrostatic inelastic compaction, that is, $\Delta(\Delta\varphi_i)/\Delta(\varepsilon_i) = 3$. Dashed tie lines connect data corresponding to the fixed values of inelastic porosity reduction indicated in black. These data are compared to the behavior implied by the modified Cam-clay yield envelopes constructed for these values of inelastic porosity reduction shown in Figure 10, assuming that the normality condition applies (grey curves). If the normality condition applies, then the grey curves and the $\Delta(\Delta\varphi_i)/\Delta(\varepsilon_i)$ versus P data obtained for the same value of $\Delta\varphi_i$ overlap, which is the case for Stage 2 data (red) only.

By contrast, the $\frac{\Delta(\Delta\varphi_i)}{\Delta(\varepsilon_i)}$ values obtained during Stage 3c deviatoric stress cycling (blue points) are higher than those predicted assuming normality at the corresponding values of P , φ_0 , and $\Delta\varphi_i$. Hence, for each increase in inelastic axial strain, more inelastic porosity reduction was seen than expected for an isotropic material (cf. Baud et al., 2006). This is in agreement with the different inelastic hardening trends shown during deviatoric versus hydrostatic compression (Figures 4a–4c) and with our microstructural evidence for strongly localized deformation in Stage 3c (Figures 8d, 9e, 9f, and S4). This confirms the inference by previous authors that localized, inelastic deformation of sandstone leads to inelastic strains that cannot be directly related to the yield envelope via the normality condition (Baud et al., 2006; Issen & Rudnicki, 2000; Rudnicki & Rice, 1975).

In summary, the presently used plasticity model, involving a modified Cam-clay yield envelope and porosity-controlled hardening behavior adequately describes the inelastic deformation behavior occurring during the near linear, Stage 2 part of the P – $\Delta\varphi_t$ curve, while the high-strain Stage 3c behavior is poorly described by this model.

7. Implications for the Groningen Gas Field

7.1. Mechanical Behavior Under In Situ Conditions

To assess the impact of current and future production strategies in producing fields, such as the Groningen gas field (Figure 1) on subsidence and induced seismicity, geomechanical models require an accurate description of the elastic versus inelastic deformation behavior, relevant for the small

strains accompanying pore pressure reduction (de Waal et al., 2015; Spiers et al., 2017). In sandstone reservoirs, the vertical strains, whether these are measured in situ (Cannon & Kole, 2017; Kole, 2015) or are inferred from surface subsidence data (Bourne et al., 2014; Mallman & Zoback, 2007; Morton et al., 2006), typically fall in the range of 0.1% to 1.0%. If we assume that any preexisting cracks present in the sandstone test samples are already closed in the reservoir, then the compliant, Stage 1 inelastic porosity reductions seen in our experiments are not expected to occur in the reservoir. The present deviatoric test data showed that during Stage 2, the changes in total axial strain ranged up to 1.0% ($\varphi_0 = 13.4\%$ – 13.9%), 0.7% ($\varphi_0 = 21.4\%$ – 21.5%), and 0.7% ($\varphi_0 = 25.6\%$ – 26.4%), while the corresponding changes in total porosity reduction ranged up to 1.1%, 1.3%, and 1.9%, respectively. The small vertical strains seen in sandstone reservoirs, notably that in Groningen (up to $\sim 0.3\%$; Cannon & Kole, 2017; NAM, 2016), fall well within these ranges for the total axial strain, suggesting that in situ compaction largely reflects Stage 2 deformation behavior. During Stage 2, inelastic porosity reductions were generally small (0.4% to 0.6%) but still constitute 30% to 50% of the total porosity reduction measured in this stage (Figure 4). In many geomechanical modelling studies (Bourne et al., 2014; Dempsey & Suckale, 2017; Lele et al., 2016; Postma & Jansen, 2018; Wassing et al., 2016; Zbinden et al., 2017), these inelastic strains are ignored, while the stress versus total strain behavior is quantified using the assumed elastic constants. We emphasize that while this assumption of poroelastic behavior in the near-linear Stage 2 may originate from the small absolute inelastic strains developing here, the relative inelastic contribution to the total deformation behavior (30%–50%) is significant and should therefore be considered alongside the elastic behavior.

In the following, we demonstrate the effect of taking into account inelastic deformation during Stage 2, on in situ stress changes, and on the partitioning of elastic strain energy available for release during fault rupture (McGarr, 1999; Shipton et al., 2013). To do so, we apply our data to the case of the seismogenic Groningen gas field in the Netherlands. We first estimate the in situ stress changes that would occur during pore pressure reduction when treating the total deformation of the reservoir as if purely poroelastic, as is often done in geomechanical studies (see Introduction). This (pseudo)-elastic base case is then compared to the behavior expected in the more realistic case where the reservoir compacts through combined elastic plus inelastic deformation, described by the Stage 2 behavior of our samples.

7.2. Stress-Strain Relations Applying During Pore Pressure Reduction

7.2.1. Poroelastic Relations

We take the Biot coefficient to be equal to 1 (i.e., similar pore and bulk volume response—see section 4.2.2) and assume that the total vertical (overburden) stress remains constant during pore pressure reduction. The incremental increase in effective vertical stress during pore pressure reduction can then be written as $d\sigma_1^{\text{eff}} = -dP_p$, where pore pressure reduction is negative. The increments in vertical elastic strain ($d\varepsilon_{el,1}$) and horizontal elastic strain ($d\varepsilon_{el,3}$) developing upon incremental changes in pore pressure and/or effective horizontal stress ($d\sigma_3^{\text{eff}}$) are then given by poroelasticity theory (Paterson & Wong, 2005; Wang, 2000) as follows:

$$d\varepsilon_{el,1} = \left(\frac{2}{9K} + \frac{2}{6G} \right) d\sigma_3^{\text{eff}} - \left(\frac{1}{9K} + \frac{2}{6G} \right) dP_p \quad (4a)$$

and

$$d\varepsilon_{el,3} = \left(\frac{2}{9K} + \frac{1}{6G} \right) d\sigma_3^{\text{eff}} - \left(\frac{1}{9K} - \frac{1}{6G} \right) dP_p \quad (4b)$$

where G is the shear modulus, relating to the bulk modulus (K), and the Young's modulus (E) through $G = 3KE/(9K - E)$. The change in the effective horizontal stress that would occur if reservoir deformation is fully elastic is given as (Zoback, 2007)

$$\Delta\sigma_3^{\text{eff}} = \alpha\Delta P_p \left(\frac{(1-2\nu)}{(1-\nu)} - 1 \right) \quad (5)$$

where ν is the Poisson's ratio, which can be obtained through $\nu = 0.5 - E/(6K)$.

Table 2
Input Parameters Used to Construct the Plots Shown in Figure 12

φ_0 (%)	E_a (GPa)	K_a (GPa)	G_a (GPa)	ν_a	E (GPa)	K (GPa)	G (GPa)	ν	$d\Delta\varphi_i/d\sigma^*$ (%/GPa)
13.4	13.8	8.3	5.6	0.22	22.0	11.0	9.4	0.17	3.6
21.5	8.6	5.7	3.4	0.25	13.7	7.8	5.7	0.21	6.0
26.4	5.7	4.1	2.2	0.27	10.1	6.2	4.1	0.23	10.3

Note. φ_0 denotes the initial porosity. E_a , K_a , G_a , and ν_a denote the apparent Young's, bulk and shear moduli, and the apparent Poisson's ratio, which are obtained from unloading P -versus total porosity reduction and from Q versus total axial strain data. E , K , G , and ν denote the truly elastic Young's bulk and shear moduli and the Poisson's ratio, respectively, and are obtained from unloading data. The $d\Delta\varphi_i/d\sigma^*$ term is the inelastic porosity reduction developing per unit increase of hydrostatic mean effective stress.

7.2.2. Plasticity Model Describing Stage 2 Behavior

We have shown that the inelastic strains developing during the Stage 2 part of the P - $\Delta\varphi_t$ curves can be described using plasticity theory combined with the modified Cam-clay yield surface. Inserting the modified Cam-clay yield function (equation (1)) into the general inelastic flow rules outlined by Muir Wood (1991, pp.107), as shown in supporting information S5, we obtain the following expressions for the increments in inelastic vertical strain ($d\varepsilon_{i,1}$) and inelastic horizontal strain ($d\varepsilon_{i,3}$) developing during incremental reductions in pore pressure and/or increases in effective horizontal stress, at any current state of differential stress (Q) and mean effective stress (P)

$$d\varepsilon_{i,1} = \frac{d\Delta\varphi_i}{d\sigma^*} \left(\left(\frac{2Q}{3PM^2} - \frac{4Q^2}{M^4P^2 - (QM)^2} + \frac{2}{9} \left(1 - \left(\frac{Q}{PM} \right)^2 \right) \right) d\sigma_3^{eff} - \left(\frac{4Q}{3PM^2} + \frac{4Q^2}{M^4P^2 - (QM)^2} + \frac{1}{9} \left(1 - \left(\frac{Q}{PM} \right)^2 \right) \right) dP_p \right) \quad (6a)$$

and:

$$d\varepsilon_{i,3} = -\frac{d\Delta\varphi_i}{d\sigma^*} \left(\left(\frac{4Q}{3PM^2} - \frac{2Q^2}{M^4P^2 - (QM)^2} - \frac{2}{9} \left(1 - \left(\frac{Q}{PM} \right)^2 \right) \right) d\sigma_3^{eff} + \left(\frac{Q}{3PM^2} - \frac{2Q^2}{M^4P^2 - (QM)^2} + \frac{1}{9} \left(1 - \left(\frac{Q}{PM} \right)^2 \right) \right) dP_p \right) \quad (6b)$$

Here $\frac{d\Delta\varphi_i}{d\sigma}$ is a factor expressing the hardening rate due to inelastic porosity reduction. Under uniaxial strain boundary conditions expected to be prevalent in the reservoir, the total horizontal strain, which is the sum of its elastic and inelastic components, must be equal to zero, so that $d\varepsilon_{tot,3} = d\varepsilon_{el,3} + d\varepsilon_{i,3} = 0$. Using this relation and equations (4b) and (6b), we obtain the change in effective horizontal stress developing as the pore pressure is reduced under uniaxial strain boundary conditions:

$$d\sigma_3^{eff} = -dP_p \frac{\left(\frac{d\Delta\varphi_i}{d\sigma} \left(\frac{Q}{3PM^2} - \frac{2Q^2}{M^4P^2 - (QM)^2} + \frac{1}{9} \left(1 - \left(\frac{Q}{PM} \right)^2 \right) \right) + \frac{1}{9K} - \frac{1}{6G} \right)}{\left(\frac{d\Delta\varphi_i}{d\sigma} \left(\frac{4Q}{3PM^2} - \frac{2Q^2}{M^4P^2 - (QM)^2} - \frac{2}{9} \left(1 - \left(\frac{Q}{PM} \right)^2 \right) \right) - \frac{2}{9K} - \frac{1}{6G} \right)} \quad (7)$$

7.3. Application to the Groningen Gas Field

We now apply the above equations to the case of the Groningen field. We assume an initial vertical effective stress of 30 MPa (Hettinga et al., 2000) and an initial horizontal effective stress of 8 MPa, as was estimated for the Groningen field by Breckels and van Eekelen (1982), meaning that the initial values of P and Q are 15.3 and 22.0 MPa, respectively. During field production, the pore pressure dropped from an initial 35 MPa to the current 8 MPa (NAM, 2016), while full depletion would mean a further drop to 0.1 MPa.

We first explore the effective horizontal stress changes that would occur for the elastic base-case scenario. The apparent bulk moduli (K_a) are equivalent to the total hardening rates (i.e., $dP/d\Delta\varphi_t$) described for Stage 2 in our hydrostatic plus deviatoric tests (see section 4.2.1) and listed in Table 2. Apparent Young's moduli are obtained using the unloading Q - ε_t data (Figures 4d-4f) measured within the same P - $\Delta\varphi_t$

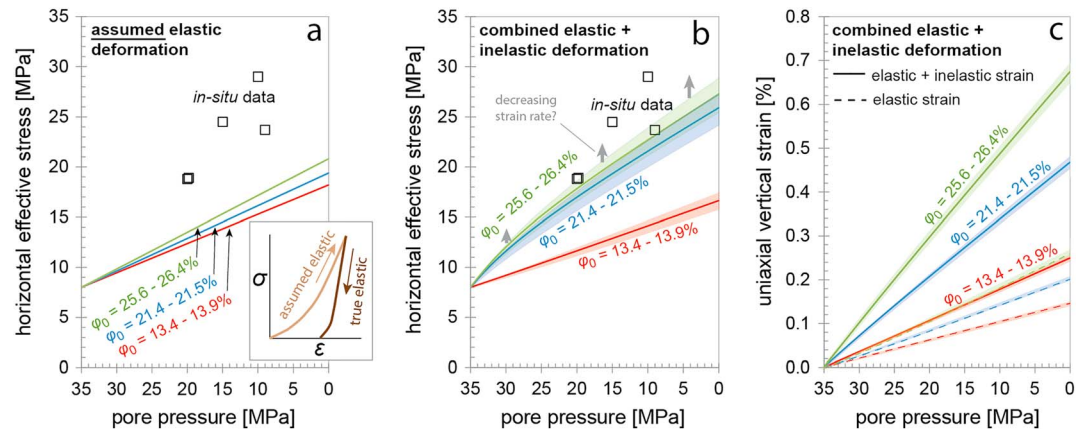


Figure 12. Plots showing the effect of the inelastic contribution to compaction of Slochteren sandstone with initial porosities (φ_0) of 13.4%–26.4%, on predicted effective horizontal stress (σ_3^{eff}) changes and elastic versus inelastic strain partitioning during pore pressure (P_p) reduction under uniaxial strain conditions. (a) Evolution of σ_3^{eff} with decreasing P_p , obtained by taking Stage 2 unloading data as if fully poroelastic (see inset). Thus, obtained stress evolutions significantly misrepresent the values measured in the field (open square symbols; van Eijs, 2015). (b) σ_3^{eff} versus P_p behaviors obtained by taking into account both the true elastic contribution (see inset (a)) and the inelastic contribution to the total deformation behavior. Shaded areas indicate the error due to the error on M of ± 0.1 . Thus, predicted $\sigma_3^{\text{eff}}-P_p$ curves are much more sensitive to φ_0 than assumed poroelastic curves (a), while higher porosity sandstones much better represent the measured in situ data. At fixed P_p , σ_3^{eff} is expected to be higher still with decreasing strain rate (grey arrows). (c) Total and elastic uniaxial vertical strain versus P_p data, predicted for combined elastic plus inelastic deformation.

interval used in determining K_a . Using K_a and E_a , we calculate the corresponding apparent shear moduli (G_a) and the apparent Poisson's ratios (ν_a —Table 2), by using the poroelastic relations between K , E , G , and ν outlined in section 7.2.1. Inserting the resultant values of ν_a into equation (5), σ_3^{eff} is shown to increase linearly with decreasing pore pressure to final values of 18, 19, and 20 MPa at a final P_p of 0.1 MPa, in low, intermediate, and high porosity sandstone, respectively. Hence, in the elastic base-case scenario, the in situ effective stress evolution shown by sandstones with a wide range of porosities (13%–26%) is expected to be similar within 1 MPa. Moreover, comparing these predicted σ_3^{eff} versus P_p data to in situ σ_3^{eff} versus P_p data (van Eijs, 2015) measured in the more porous parts of the field (mean $\varphi > 18\%$), it is evident from Figure 12a that the change in σ_3^{eff} expected for an elastically deforming reservoir grossly underestimates the measured values by 5 to 12 MPa, that is, by 30% to 60% of the increase in σ_3^{eff} .

We now consider the more realistic case where pore pressure reduction leads to combined elastic plus inelastic Stage 2 deformation of the reservoir sandstone. To represent the elastic strain and stress changes developing in situ, we use values of the (true elastic) bulk modulus (K) and Young's modulus (E) obtained from our unloading data at $P = 50$ MPa, $P_c^{\text{eff}} = 40$ MPa, and $Q = 30$ MPa. The K and E values obtained, and the corresponding calculated values of G and ν are listed in Table 2. Values of M were obtained at the same stress conditions, that is, from the lowest inelastic porosity reduction contours to which Cam-clay yield envelopes were fitted (Figure 10). For simplicity, M is assumed to remain constant during deformation, which is a reasonable approximation provided inelastic porosity reductions are small ($< 0.3\%$). The inelastic hardening factors $\frac{d\Delta\varphi_i}{d\sigma_3^{\text{eff}}}$ are equal to the inverse of the inelastic hardening rates ($dP/d\Delta\varphi_i$ —similar values in Stage 2 deviatoric and hydrostatic compression) given in section 4.2.1 and are listed in Table 2. Inserting these values of K , G , M , and $\frac{d\Delta\varphi_i}{d\sigma_3^{\text{eff}}}$ into equation (7), we calculate the effective horizontal stress increments ($d\sigma_3^{\text{eff}}$) developing during successive pore pressure reduction increments (dP_p) of -0.1 MPa, recomputing the new σ_3^{eff} , Q , and P after each increment. For the stress changes obtained, the corresponding increments of elastic ($d\varepsilon_{e1,1}$) and inelastic vertical strain increments ($d\varepsilon_{i1,1}$), are calculated using equations (4a) and (6a), respectively. The cumulative elastic vertical strain ($\varepsilon_{e1,1}$) and cumulative inelastic vertical strain ($\varepsilon_{i1,1}$) are each the sum of their preceding increments, while the total, uniaxial vertical strain is given as the sum of these cumulative elastic and inelastic components ($\varepsilon_{e1,1} + \varepsilon_{i1,1}$). The resulting predicted $\sigma_3^{\text{eff}}-P_p$ behaviors and total and elastic strain versus P_p curves are shown in Figures 12b and 12c, respectively.

In Figure 12b, the shaded fields around the solid lines show the error in σ_3^{eff} due to the error in M of ± 0.1 . The horizontal effective stress increases nonlinearly with decreasing pore pressure. For low porosities, the evolution of σ_3^{eff} with decreasing pore pressure is similar to the behavior seen in the elastic base-case (Figure 12a). By contrast, for higher porosities, markedly higher effective horizontal stresses are seen, where at full depletion, $\sigma_3^{\text{eff}} = 24.0 \pm 1.2$ MPa ($\varphi_0 = 21.4\%–21.5\%$) and 26.0 ± 1.5 MPa ($\varphi_0 = 25.6\%–26.4\%$). These values are much closer (within 1–5 MPa) to the in situ data measured at the same pore pressure in the high porosity ($\varphi > 20\%$) regions of the reservoir, than obtained assuming purely elastic behavior (compare Figures 12a and 12b).

Note that the present experimental data used to fit the above plasticity model were obtained at strain and loading rates ($\dot{\epsilon}_t \sim 10^{-5} \text{ s}^{-1}$; $\dot{P} \sim 0.1 \text{ MPa s}^{-1}$) that are significantly faster than the strain-rates of $\sim 10^{-12} \text{ s}^{-1}$ inferred in the reservoir over decades of production (Cannon & Kole, 2017). In previous experiments on Slochteren sandstone, strain rates down to 10^{-10} s^{-1} were explored over the timescale of a week (Pijenburg et al., 2018), or down to 10^{-11} s^{-1} over several months (Hol et al., 2015), during which the inelastic contribution to the total axial strain measured increased by 10% to 20%. Therefore, at the strain rates of 10^{-12} s^{-1} inferred for the Groningen gas field (Cannon & Kole, 2017) and for other fields (Mallman & Zoback, 2007; Morton et al., 2001), inelastic deformation may play an even larger role than represented in Figure 12 for Groningen, causing a larger increase in σ_3^{eff} with decreasing P_p (grey arrows in Figure 12b). We therefore suggest that the in situ stress evolution in Groningen and other hydrocarbon fields is best represented by taking into account not only the elastic and inelastic contributions to deformation, but also any rate-sensitivity of the latter (cf. Pijenburg et al., 2018).

At full depletion, the total, uniaxial vertical strains obtained for low, intermediate, and high porosity sandstones are, respectively, $0.23\% \pm 0.05\%$, $0.45\% \pm 0.1\%$, and $0.66\% \pm 0.1\%$, to which elastic deformation contributes $0.15\% \pm 0.02\%$, $0.22\% \pm 0.05\%$, and $0.28\% \pm 0.05\%$, respectively (Figure 12c). Hence, based on these data, 30% to 50% of the total strain energy accumulating during pore pressure reduction is inelastic, hence dissipated (cf. Hol et al., 2018; Pijenburg et al., 2018). This is then unavailable for release during fault rupture through seismicity and associated processes, such as frictional heating, fault asperity breakage, wall-rock damage, pore pressure changes, and fluid flow (Cooke & Madden, 2014; Mcgarr, 1999; Shipton et al., 2013). Finally, we note that the marked, porosity-sensitive behavior shown by the horizontal stress evolution and by elastic and inelastic deformation imply that different compaction behavior and associated stress changes can be expected in a field like the Groningen field, where different parts of the reservoir are characterized by markedly different mean porosities (Figure 1b). We accordingly believe that incorporating inelastic deformation into geomechanical modelling of fields such as Groningen will have significant impact on model outcomes on compaction, subsidence, stress evolution, fault reactivation, and induced seismicity.

8. Conclusions

In this study, we quantified the elastic and inelastic contributions to the total deformation behavior of Slochteren sandstones from the currently producing, seismogenic Groningen gas field in the Netherlands (Figure 1). This was done by performing hydrostatic and deviatoric stress cycling experiments under conditions of temperature ($T = 100 \text{ }^\circ\text{C}$) and pore fluid chemistry ($\sim 4 \text{ M}$ saline brine) relevant for the top of the Slochteren reservoir. A wide range of stress changes was employed to include the stress conditions relevant for fluid extraction from reservoirs at depths up to 5 km and to cover the Stages 1, 2, and 3d or 3c $P-\Delta\varphi_t$ behavior (cf. Figure 2), in all our samples. Thus, we explored hydrostatic mean effective stresses up to $P = 320$ MPa, differential stresses up to $Q = 135$ MPa, pore pressure of 0.1 or 1.0 MPa, and initial sample porosities (φ_0) of 13.4% to 26.4%, covering the porosity range in the field. An axial strain rate of 10^{-5} s^{-1} and a loading rate of $\sim 0.1 \text{ MPa/s}$ were used. We concluded the following points:

1. Stress cycling did not affect the overall mechanical behavior of our samples (Figure 3).
2. Mean effective stress versus total (elastic + inelastic) porosity reduction data obtained in the present combined hydrostatic plus deviatoric stress cycling tests (Figure 4), and in hydrostatic (Rene), stress cycling tests (Figure 6) show typical Stages 1, 2, and 3d or 3c behavior as often described in the literature (cf. Figure 2).

3. Inelastic deformation contributes to 30% to 50% of the total porosity reduction at each stage, including the near-linear Stage 2, which has been often assumed to be fully poroelastic. The inelastic contribution was larger in higher porosity samples.
4. The elastic bulk moduli (K) and Young's moduli (E) both showed a monotonic increase with increasing P and φ_0 (Figure 5). At $P \leq 30$ MPa, K values obtained during deviatoric unloading were larger by 1–2 GPa than the values obtained during hydrostatic unloading, implying anisotropic behavior at these low stresses. At $P = 50$ –85 MPa, K values showed more isotropic behavior.
5. Quantitative microstructural investigation showed that the role played by intragranular cracking in accommodating the inelastic deformations measured in reference samples deformed up to Stages 1, 2, and 3c (Figure 7) was negligible, small, and large, respectively (Figure 8), as implied by the obtained, stage-specific changes in mean crack density per unit porosity reduction of 1.1, 32.4, and 110.7 mm⁻²%, respectively.
6. Therefore, the small, inelastic strains developing during Stage 2, expected to be relevant for sandstone reservoirs undergoing pore pressure reduction are thought to be largely accommodated by intergranular displacements developing normal and parallel to grain contacts that are weakly sutured, and/or clay filled (e.g., Figures 9b and 9d), with a smaller role played by intragranular cracking. Intragranular cracking was found to be more significant during nonlinear, Stages 3d (dilatant) and 3c (nonlinear compactant) P - $\Delta\varphi_t$ behavior (Figures 8d and 9f).
7. Stage 2 inelastic behavior was demonstrated to be well described by a plasticity model that utilizes the modified Cam-clay yield function (Figure 10), while obeying the normality condition (Figure 11), thus implying isotropic behavior. This was not the case for the inelastic strains developing during Stages 3d and 3c.
8. We applied this plasticity model in combination with poroelasticity theory to the case of the Groningen gas field. It was shown that the in situ effective horizontal stress versus pore pressure data measured in the reservoir were far better represented by this combined elastic plus inelastic model (up to 40% difference) than they were by assuming that the total behavior could be described using poroelasticity. This was particularly apparent in the higher porosity materials ($\varphi_0 \geq 21.4\%$).
9. Under modelled, uniaxial strain boundary conditions, again 30% to 50% of the total vertical strain was found to be inelastic (i.e., dissipated) and is therefore unavailable for release through seismicity and associated fault rupture processes. This effect is larger in higher porosity sandstones and is expected to be larger still with decreasing strain rate.
10. Our results indicate that markedly different stress evolutions may be expected across a field characterized by nonuniform porosity, such as the Groningen field (Figure 1b). Therefore, taking into account the inelastic contribution to the total deformation of reservoir sandstone has a key role to play in future geo-mechanical modelling of induced seismicity and subsidence.

Acknowledgments

This research was carried out in the context of the research program funded by the Nederlandse Aardolie Maatschappij (NAM). This program aims to fundamentally improve understanding of production-induced reservoir compaction and seismicity in the seismogenic Groningen gas field. We thank the teams at NAM and Shell Global Solutions for providing samples and data and NAM for allowance to publish this study. Specifically, the authors like to thank Dirk Doornhof, Rob van Eijs (both NAM), and two anonymous reviewers for their help in improving the quality of the manuscript. Colin Peach is thanked for advice and help both inside and outside of the lab. We thank UU employees Gert Kastelein, Thony van der Gonnetscher, and Floris van Oort for technical assistance and Maartje Hamers for acquiring several of the micrographs used in this study. The data used in this paper are available as Pijnenburg et al. (2019): Mechanical and microstructural data used in: "Inelastic deformation of the Slochteren sandstone: Stress-strain relations and implications for induced seismicity in the Groningen gas field." GFZ Data Services (<http://doi.org/10.5880/figeo.2019.013>).

References

- Amthor, J. E., & Okkerman, J. (1998). Influence of early diagenesis on reservoir quality of Rotliegend sandstones, Northern Netherlands. *American Association of Petroleum Geologists Bulletin*, 82, 2246–2265.
- Baud, P., Klein, E., & Wong, T. (2004). Compaction localization in porous sandstones: Spatial evolution of damage and acoustic emission activity. *Journal of Structural Geology*, 26(4), 603–624. <https://doi.org/10.1016/j.jsg.2003.09.002>
- Baud, P., Vajdova, V., & Wong, T. F. (2006). Shear-enhanced compaction and strain localization: Inelastic deformation and constitutive modeling of four porous sandstones. *Journal of Geophysical Research*, 111, B12401. <https://doi.org/10.1029/2005JB004101>
- Baud, P., Zhu, W., & Wong, T. (2000). Failure mode and weakening effect of water on sandstone. *Journal of Geophysical Research*, 105, 371–389. <https://doi.org/10.1029/2000JB900087>
- Bedford, J. D., Faulkner, D. R., Leclère, H., & Wheeler, J. (2018). High-resolution mapping of yield curve shape and evolution for porous rock: The effect of inelastic compaction on porous bassanite. *Journal of Geophysical Research: Solid Earth*, 123, 1217–1234. <https://doi.org/10.1002/2017JB015250>
- Bernabe, Y., Fryer, D. T., & Shively, R. M. (1994). Experimental-observations of the elastic and inelastic behavior of porous sandstones. *Geophysical Journal International*, 117, 403–418.
- Blöcher, G., Reinsch, T., Hassanzadegan, A., Milsch, H., & Zimmermann, G. (2014). Direct and indirect laboratory measurements of poroelastic properties of two consolidated sandstones. *International Journal of Rock Mechanics and Mining Sciences*, 67, 191–201. <https://doi.org/10.1016/j.ijrmms.2013.08.033>
- Bourne, S. J., Oates, S. J., van Elk, J., & Doornhof, D. (2014). A seismological model for earthquakes induced by fluid extraction from a subsurface reservoir. *Journal of Geophysical Research: Solid Earth*, 119, 8991–9015. <https://doi.org/10.1002/2014JB011663>
- Brantut, N., Heap, M. J., Baud, P., & Meredith, P. G. (2014). Rate- and strain-dependent brittle deformation of rocks. *Journal of Geophysical Research: Solid Earth*, 119, 1818–1836. <https://doi.org/10.1002/2013JB010448>
- Brantut, N., Heap, M. J., Meredith, P. G., & Baud, P. (2013). Time-dependent cracking and brittle creep in crustal rocks: A review. *Journal of Structural Geology*, 52, 17–43. <https://doi.org/10.1016/j.jsg.2013.03.007>

- Breckels, I. M., & van Eekelen, H. A. M. (1982). Relationship between horizontal stress and depth in sedimentary basins. *Journal of Petroleum Technology*, 34, 2191–2199. <https://doi.org/10.2118/10336-PA>
- Buijze, L., van den Bogert, P. A. J., Wassing, B. B. T., Orlic, B., & Ten Veen, J. (2017). Fault reactivation mechanisms and dynamic rupture modelling of depletion-induced seismic events in a Rotliegend gas reservoir. *Geologie en Mijnbouw/Netherlands Journal of Geosciences*, 96(5), s131–s148. <https://doi.org/10.1017/njg.2017.27>
- Cannon, M., & Kole, P. (2017). *The First Year of Distributed Strain Sensing (DSS) Monitoring in the Groningen Gas Field*. Shell International Exploration and Production Inc., Houston.
- Chan, A. W., Hagin, P. N., & Zoback, M. D. (2004). Viscoplastic deformation in unconsolidated reservoir sands: Field applications using dynamic DARS analysis, ARMA/NARMS.
- Chang, C., Zoback, M. D., & Khaksar, A. (2006). Empirical relations between rock strength and physical properties in sedimentary rocks. *Journal of Petroleum Science and Engineering*, 51, 223–237. <https://doi.org/10.1016/j.petrol.2006.01.003>
- Chester, J. S., Lenz, S. C., Chester, F. M., & Lang, R. a. (2004). Mechanisms of compaction of quartz sand at diagenetic conditions. *Earth and Planetary Science Letters*, 220, 435–451. [https://doi.org/10.1016/S0012-821X\(04\)00054-8](https://doi.org/10.1016/S0012-821X(04)00054-8)
- Cooke, M. L., & Madden, E. H. (2014). Is the Earth lazy? A review of work minimization in fault evolution. *Journal of Structural Geology*, 66, 334–346. <https://doi.org/10.1016/j.jsg.2014.05.004>
- Crawford, B. R., Sanz, P. F., Alramahi, B., & DeDontney, N. L. (2011). Modeling and prediction of formation compressibility and compactive pore collapse in siliciclastic rocks, ARMA 45th US Rock Mech./Geomech. Symp., 11(384).
- Crawford, B. R., & Yale, D. P. (2002). Constitutive modeling of deformation and permeability: Relationships between critical state and micromechanics, Proc. SPE/ISRM Rock Mech. Conf., <https://doi.org/10.2118/78189-MS>
- Curran, J. H., & Carroll, M. M. (1979). Shear stress enhancement of void compaction. *Journal of Geophysical Research*, 84(B3), 1105–1112. <https://doi.org/10.1029/JB084iB03p01105>
- David, E. C., Brantut, N., Schubnel, A., & Zimmerman, R. W. (2012). Sliding crack model for nonlinearity and hysteresis in the uniaxial stress-strain curve of rock. *International Journal of Rock Mechanics and Mining Sciences*, 52, 9–17. <https://doi.org/10.1016/j.ijrmms.2012.02.001>
- Dempsey, D., & Suckale, J. (2017). Physics-based forecasting of induced seismicity at Groningen gas field, the Netherlands. *Geophysical Research Letters*, 44, 7773–7782. <https://doi.org/10.1002/2017GL073878>
- Desai, C. S., & Siriwardane, H. J. (1984). *Constitutive Laws for Engineering Materials: With Emphasis on Geological Materials*. Englewood Cliffs, New Jersey: Prentice-Hall.
- de Waal, J. A., Muntendam-Bos, A. G., & Roest, J. P. A. (2015). Production induced subsidence and seismicity in the Groningen gas field—Can it be managed? *Proceedings of the International Association of Hydrological Sciences*, 372, 129–139. <https://doi.org/10.5194/piahs-372-129-2015>
- Digby, P. J. (1981). The effective elastic moduli of porous granular rocks. *Journal of Applied Mechanics*, 48(4), 803. <https://doi.org/10.1115/1.3157738>
- DiGiovanni, A. A., Fredrich, J. T., Holcomb, D. J., & Olsson, W. A. (2007). Microscale damage evolution in compacting sandstone. *Geological Society of London, Special Publication*, 289(1), 89–103. <https://doi.org/10.1144/SP289.6>
- DiMaggio, F. L., & Sandler, I. S. (1971). Material model for granular soils. *Journal of the Engineering Mechanics Division*, 97(3), 935–950.
- Dost, B., & Kraaijpoel, D. (2013). *The August 16, 2012 Earthquake Near Huizinge (Groningen)*. De Bilt: KNMI.
- van Eijs, R. M. H. E., Mulders, F. M. M., Nepveu, M., Kenter, C. J., & Scheffers, B. C. (2006). Correlation between hydrocarbon reservoir properties and induced seismicity in the Netherlands. *Engineering Geology*, 84(3–4), 99–111. <https://doi.org/10.1016/j.enggeo.2006.01.002>
- Evans, K. F., Zappone, A., Kraft, T., Deichmann, N., & Moia, F. (2012). A survey of the induced seismic responses to fluid injection in geothermal and CO₂ reservoirs in Europe. *Geothermics*, 41, 30–54. <https://doi.org/10.1016/j.geothermics.2011.08.002>
- Fialko, Y., & Simons, M. (2000). Deformation and seismicity in the Coso geothermal area, Inyo County, California: Observations and modeling using satellite radar interferometry. *Journal of Geophysical Research*, 105(B9), 21,781–21,793. <https://doi.org/10.1029/2000JB900169>
- Fortin, J., Schubnel, A., & Guéguen, Y. (2005). Elastic wave velocities and permeability evolution during compaction of Bleurswiller sandstone. *International Journal of Rock Mechanics and Mining Sciences*, 42(7–8), 873–889. <https://doi.org/10.1016/j.ijrmms.2005.05.002>
- Fortin, J., Stanchits, S., Dresen, G., & Guéguen, Y. (2006). Acoustic emission and velocities associated with the formation of compaction bands in sandstone. *Journal of Geophysical Research*, 111, B10203. <https://doi.org/10.1029/2005JB003854>
- Fredrich, J. T., & Fossum, A. F. (2002). Large-scale three-dimensional geomechanical modeling of reservoirs: Examples from California and the deepwater Gulf of Mexico. *Oil & Gas Science and Technology*, 57(5), 423–441. <https://doi.org/10.2516/ogst:2002028>
- Gaupp, R., Matter, A., Platt, J., Ramseier, K., & Walzebeck, J. (1993). Diagenesis and fluid evolution of deeply buried Permian (Rotliegendes) gas reservoirs, northwest Germany. *American Association of Petroleum Geologists Bulletin*, 77. <https://doi.org/10.1306/BDF8E0C-1718-11D7-8645000102C1865D>
- Grotsch, J., Sluijk, A., van Ojik, K., de Keijzerm, M., Graaf, J., & Steenbrink, J. (2011). The Groningen gas field: Fifty years of exploration and gas production from a Permian dryland reservoir. In R. G. J. Grötsch (Ed.), *The Permian Rotliegend of the Netherlands* (Vol. 98, pp. 11–33). Tulsa: Society for Sedimentary Geology.
- Grünthal, G. (2014). Induced seismicity related to geothermal projects versus natural tectonic earthquakes and other types of induced seismic events in Central Europe. *Geothermics*, 52, 22–35. <https://doi.org/10.1016/j.geothermics.2013.09.009>
- Guéguen, Y., & Fortin, J. (2013). Elastic envelopes of porous sandstones. *Geophysical Research Letters*, 40, 3550–3555. <https://doi.org/10.1002/grl.50676>
- Han, G., Stone, T., Liu, Q., Cook, J., & Papanastasiou, P. (2005). 3-D elastoplastic FEM modelling in a reservoir simulator, Proceedings - SPE Reservoir Simulation Symposium, 9–19.
- Heap, M. J., Baud, P., Meredith, P. G., Bell, A. F., & Main, I. G. (2009). Time-dependent brittle creep in Darley Dale sandstone. *Journal of Geophysical Research*, 114, B07203. <https://doi.org/10.1029/2008JB006212>
- Heap, M. J., Brantut, N., Baud, P., & Meredith, P. G. (2015). Time-dependent compaction band formation in sandstone. *Journal of Geophysical Research: Solid Earth*, 120, 4808–4830. <https://doi.org/10.1002/2015JB012022>
- Heap, M. J., Faulkner, D. R., Meredith, P. G., & Vinciguerra, S. (2010). Elastic moduli evolution and accompanying stress changes with increasing crack damage: Implications for stress changes around fault zones and volcanoes during deformation. *Geophysical Journal International*, 183(1), 225–236. <https://doi.org/10.1111/j.1365-246X.2010.04726.x>
- Hettema, M., Schutjens, P. M., Verboom, B., & Gussinklo, H. (2000). Production-induced compaction of a sandstone reservoir: The strong influence of stress path. *SPE Reservoir Evaluation & Engineering*, 3(4), 342–347. <https://doi.org/10.2118/65410-PA>

- Hol, S., Mossop, A. P., van der Linden, A. J., Zuiderwijk, P. M. M., & Makurat, A. H. (2015). Long-term compaction behavior of Permian sandstones—An investigation into the mechanisms of subsidence in the Dutch Wadden Sea, ARMA, 15–618.
- Hol, S., van der Linden, A., Bierman, S., Marcelis, F., & Makurat, A. (2018). Rock physical controls on production-induced compaction in the Groningen field, Sci. Rep.
- Holt, R. M., Brignoli, M., & Kenter, C. J. (2000). Core quality: Quantification of coring-induced rock alteration. *International Journal of Rock Mechanics and Mining Sciences*, 37, 889–907. [https://doi.org/10.1016/S1365-1609\(00\)00009-5](https://doi.org/10.1016/S1365-1609(00)00009-5)
- Ingraham, M. D., Bauer, S. J., Issen, K. A., & Dewers, T. A. (2017). Evolution of permeability and Biot coefficient at high mean stresses in high porosity sandstone. *International Journal of Rock Mechanics and Mining Sciences*, 96, 1–10. <https://doi.org/10.1016/j.ijrmms.2017.04.004>
- Issen, K., & Rudnicki, J. (2000). Conditions for compaction bands in porous rock. *Journal of Geophysical Research*, 105(B9), 21,529–21,536. <https://doi.org/10.1029/2000JB900185>
- Karner, S. L., Chester, J. S., Chester, F. M., Kronenberg, A. K., & Hajash, A. (2005). Laboratory deformation of granular quartz sand: Implications for the burial of clastic rocks. *American Association of Petroleum Geologists Bulletin*, 89(5), 603–625. <https://doi.org/10.1306/12200404010>
- Ketelaar, V. B. H. (2009). In F. D. van der Meer, & A. Marcal (Eds.), *Satellite Radar Interferometry: Subsidence Monitoring Techniques*. New York City: Springer.
- Klein, E., Baud, P., Reuschle, T., & Wong, T. (2001). Mechanical behaviour and failure mode of Bentheim Sandstone under triaxial compression. *Physics and Chemistry of the Earth*, 26(1–2), 21–25.
- Kole, P. (2015). In - situ compaction measurements using gamma ray markers (June).
- Lele, S., Y.-S. Hsu, J. L. Garzon, N. DeDontney, K. H. Searles, G. A. Gist, et al. (2016). Geomechanical modeling to evaluate production-induced seismicity at the Groningen field, SPE Int., (183554).
- Mallman, E. P., & Zoback, M. D. (2007). Subsidence in the Louisiana coastal zone due to hydrocarbon production. *Journal of Coastal Research*, 23(3), 771–786. <https://doi.org/10.2112/05-0553>
- McGarr, A. (1999). On relating apparent stress to the stress causing earthquake fault slip. *Journal of Geophysical Research*, 104(B2), 3003–3011. <https://doi.org/10.1029/1998JB900083>
- Menéndez, B., Zhu, W., & Wong, T.-F. (1996). Micromechanics of brittle faulting and cataclastic flow in Berea sandstone. *Journal of Structural Geology*, 18(1), 1–16. [https://doi.org/10.1016/0191-8141\(95\)00076-P](https://doi.org/10.1016/0191-8141(95)00076-P)
- Morton, R. A., Bernier, J. C., & Barras, J. A. (2006). Evidence of regional subsidence and associated interior wetland loss induced by hydrocarbon production, Gulf Coast region, USA. *Environmental Geology*, 50(2), 261–274. <https://doi.org/10.1007/s00254-006-0207-3>
- Morton, R. A., Purcell, N. A., & Peterson, R. (2001). Field evidence of subsidence and faulting induced by hydrocarbon production in coastal southeast Texas, Gulf Coast Assoc. *Transactions of the Geological Society*, 11, 239–248.
- Muir Wood, D. (1991). *Soil Behaviour and Critical State Soil Mechanics*. Cambridge, UK: Cambridge University Press.
- Mulders, F. M. M. (2003). *Modelling of Stress Development and Fault Slip In and Around a Producing Gas Reservoir*. Delft, the Netherlands: Delft University.
- NAM (2013). Technical addendum to the Winningsplan Groningen 2013 subsidence, induced earthquakes and seismic hazard analysis in the Groningen field.
- NAM (2015). *Bodemdalings door Aardgaswinning*. Friesland, en het noorden van Drenthe: NAM-gasvelden in Groningen.
- NAM (2016). Technical addendum to the Winningsplan Groningen 2016.
- Niemeijer, A. R., Spiers, C. J., & Bos, B. (2002). Compaction creep of quartz sand at 400 ^ 600³C: Experimental evidence for dissolution-controlled pressure solution. *Earth and Planetary Science Letters*, 195, 261–275.
- Paterson, M. S., & Wong, T. F. (2005). *Experimental Rock Deformation—The Brittle Field*. New York City: Springer.
- Peach, C. J. (1991). *Influence of Deformation on the Fluid Transport Properties of Salt Rocks*. Utrecht, the Netherlands: Utrecht University.
- Pijenburg, R. P. J., Verberne, B. A., Hangx, S. J. T., & Spiers, C. J. (2018). Deformation behaviour of sandstones from the seismogenic Groningen gas field: Role of inelastic versus elastic mechanisms. *Journal of Geophysical Research: Solid Earth*, 123, 5532–5558. <https://doi.org/10.1029/2018JB015673>
- Postma, T., & Jansen, J. D. (2018). The small effect of poroelastic pressure transients on triggering of production-induced earthquakes in the Groningen natural gas field. *Journal of Geophysical Research: Solid Earth*, 123, 401–417. <https://doi.org/10.1002/2017JB014809>
- Pratt, W. E., & Johnson, D. W. (1926). Local subsidence of the Goose creek oil field. *Journal of Geology*, 14(7), 945–968. <https://doi.org/10.1086/521238>
- Preibisch, S., Saalfeld, S., & Tomancak, P. (2009). Globally optimal stitching of tiled 3D microscopic image acquisitions. *Bioinformatics*, 25(11), 1463–1465. <https://doi.org/10.1093/bioinformatics/btp184>
- Renard, F., Cordonnier, B., Kobchenko, M., Kandula, N., Weiss, J., & Zhu, W. (2017). Microscale characterization of rupture nucleation unravels precursors to faulting in rocks. *Earth and Planetary Science Letters*, 476, 69–78. <https://doi.org/10.1016/j.epsl.2017.08.002>
- Renard, F., Park, A., Ortoleva, P., & Gratier, J. P. (1999). An integrated model for transitional pressure solution in sandstones. *Tectonophysics*, 312(2–4), 97–115. [https://doi.org/10.1016/S0040-1951\(99\)00202-4](https://doi.org/10.1016/S0040-1951(99)00202-4)
- Rudnicki, J. W., & Rice, J. R. (1975). Conditions for the localization of deformation in pressure-sensitive dilatant materials. *Journal of the Mechanics and Physics of Solids*, 23(6), 371–394. [https://doi.org/10.1016/0022-5096\(75\)90001-0](https://doi.org/10.1016/0022-5096(75)90001-0)
- Rutter, E. H., & Glover, C. T. (2012). The deformation of porous sandstones: Are Byerlee friction and the critical state line equivalent? *Journal of Structural Geology*, 44, 129–140.
- Sakic, A., Nanver, L. K., van Veen, G., Kooijman, K., Vogelsang, P., Scholtes, T. L. M., et al. (2011). Solid-state backscattered-electron detector for sub-keV imaging in scanning electron microscopy. In *ICT Open: Micro Technology and Micro Devices SAFE*, (pp. 1–4). Veldhoven: Technology Foundation STW.
- Santarelli, F. J., & Dusseault, M. B. (1991). Core quality control in petroleum engineering. In J. C. Roegiers (Ed.), *Rock Mechanics as a Multidisciplinary Science* (pp. 111–120). Rotterdam: Balkema.
- Schofield, A., & Wroth, P. (1968). Critical state soil mechanics. *Soil Use and Management*, 25(3), 128–105. <https://doi.org/10.1111/j.1475-2743.1987.tb00718.x>
- Schultz, R. a., & Siddharthan, R. (2005). A general framework for the occurrence and faulting of deformation bands in porous granular rocks. *Tectonophysics*, 411(1–4), 1–18. <https://doi.org/10.1016/j.tecto.2005.07.008>
- Schutjens, P. M. T. M., Hanssen, T. H., Hettema, M. H. H., Merour, J., de Bree, P., W, J., et al. (2004). Compaction-induced porosity/permeability reduction in sandstone reservoirs: Data and model for elasticity-dominated deformation. *SPE Reservoir Evaluation & Engineering*, 7(3), 202–216. <https://doi.org/10.2118/88441-PA>

- Shah, K. R., & Wong, T.-F. (1997). Fracturing at contact surfaces subjected to normal and tangential loads. *International Journal of Rock Mechanics and Mining Sciences*, 34(5), 727–739. [https://doi.org/10.1016/S1365-1609\(97\)00007-7](https://doi.org/10.1016/S1365-1609(97)00007-7)
- Shipton, Z. K., Evans, J. P., Abercrombie, R. E., & Brodsky, E. E. (2013). The missing sinks: slip localization in faults, damage zones, and the seismic energy budget. In R. Abercrombie, A. McGarr, G. Di Toro, & K. Hiroo (Eds.), *Earthquakes: Radiated Energy and the Physics of Faulting*, (pp. 217–222). Washington, DC: American Geophysical Union.
- Skurtveit, E., Torabi, A., Gabrielsen, R. H., & Zoback, M. D. (2013). Experimental investigation of deformation mechanisms during shear-enhanced compaction in poorly lithified sandstone and sand. *Journal of Geophysical Research: Solid Earth*, 118, 4083–4100. <https://doi.org/10.1002/jgrb.50342>
- Spiers, C. J., De Meer, S., Niemeijer, A. R., & Zhang, X. (2004). Kinetics of rock deformation by pressure solution and the role of thin aqueous films. In S. Nakashima, C. J. Spiers, L. Mercury, P. A. Fenter, & J. M. F. Hochella (Eds.), *Physicochemistry of Water in Geological and Biological Systems, Frontiers Science Series*, (pp. 129–158). Tokyo, Japan: Univerisal Academy Press, Inc.
- Spiers, C. J., Hangx, S. J. T., & Niemeijer, A. R. (2017). New approaches in experimental research on rock and fault behaviour in the Groningen gas field. *Netherlands Journal of Geosciences*, 96(05), s55–s69. <https://doi.org/10.1017/njg.2017.32>
- Tembe, S., Baud, P., & Wong, T. F. (2008). Stress conditions for the propagation of discrete compaction bands in porous sandstone. *Journal of Geophysical Research*, 113, B09409. <https://doi.org/10.1029/2007JB005439>
- Tembe, S., Vajdova, V., Baud, P., Zhu, W., & fong Wong, T. (2007). A new methodology to delineate the compactive yield cap of two porous sandstones under undrained condition. *Mechanics of Materials*, 39(5), 513–523. <https://doi.org/10.1016/j.mechmat.2006.08.005>
- van Eijs, R. (2015). Neotectonic stresses in the Permian Slochteren Formation of the Groningen field. KNMI Scientific Report No. EP201510210531.
- van Noort, R., Visser, H. J. M., & Spiers, C. J. (2008). Influence of grain boundary structure on dissolution controlled pressure solution and retarding effects of grain boundary healing. *Journal of Geophysical Research*, 113, B03201. <https://doi.org/10.1029/2007JB005223>
- van Wees, J. D., Buijze, L., van Thienen-Visser, K., Nepveu, M., Wassing, B. B. T., Orlic, B., & Fokker, P. A. (2014). Geomechanics response and induced seismicity during gas field depletion in the Netherlands. *Geothermics*, 52, 206–219. <https://doi.org/10.1016/j.geothermics.2014.05.004>
- Waldmann, S. (2011). *Geological and Mineralogical Investigation of Rotliegend Gas Reservoirs in the Netherlands and their Potential for CO₂ Storage*. Jena: Jena University.
- Waldmann, S., Busch, A., van Ojik, K., & Gaupp, R. (2014). Importance of mineral surface areas in Rotliegend sandstones for modeling CO₂-water-rock interactions. *Chemical Geology*, 378–379(1), 89–109. <https://doi.org/10.1016/j.chemgeo.2014.03.014>
- Waldmann, S., & Gaupp, R. (2016). Grain-rimming kaolinite in Permian Rotliegend reservoir rocks. *Sedimentary Geology*, 335, 17–33. <https://doi.org/10.1016/j.sedgeo.2016.01.016>
- Walsh, J. B. (1965). The effect of cracks on the compressibility of rock. *Journal of Geophysical Research*, 70(2), 381–389. <https://doi.org/10.1029/JZ070i002p00381>
- Walton, K. (1987). The effective elastic moduli of a random packing of spheres. *Journal of the Mechanics and Physics of Solids*, 35(2), 213–226. [https://doi.org/10.1016/0022-5096\(87\)90036-6](https://doi.org/10.1016/0022-5096(87)90036-6)
- Wang, H. F. (2000). *Theory of Linear Poroelasticity with Applications to Geomechanics and Hydrogeology*. Mercer County, New Jersey: Princeton Univ. Press.
- Wassing, B. B. T., Buijze, L., & Orlic, B. (2016). Modelling of fault reactivation and fault slip in producing gas fields using a slip-weakening friction law, 50th US Rock Mech. /Geomech. Symp.
- Wilson, M. D. (1992). Inherited grain-rimming clays in sandstones from Eoilian and shelf environments: Their origin and control on reservoir properties. *Society for Sedimentary Geology*.
- Wong, T. F., & Baud, P. (1999). Mechanical compaction of porous sandstone. *Oil & Gas Science and Technology*, 54(6), 715–727. <https://doi.org/10.2516/ogst:1999061>
- Wong, T. F., & Baud, P. (2012). The brittle-ductile transition in porous rock: A review. *Journal of Structural Geology*, 44, 25–53. <https://doi.org/10.1016/j.jsg.2012.07.010>
- Wong, T. F., Christian, D., & Wenlu, Z. (1997). The transition from brittle faulting to cataclastic flow in porous sandstones: Mechanical deformation. *Journal of Geophysical Research*, 102, 3009–3025. <https://doi.org/10.1029/96JB03281>
- Wong, T.-F., Szeto, H., & Zhang, J. (1992). Effect of loading path and porosity on the failure mode of porous rocks. *Applied Mechanics Reviews*, 45(8), 281–293. <https://doi.org/10.1115/1.3119759>
- Wu, X. Y., Baud, P., & Wong, T. (2000). Micromechanics of compressive failure and spatial evolution of anisotropic damage in Darley Dale sandstone. *International Journal of Rock Mechanics and Mining Sciences*, 37(1–2), 143–160. [https://doi.org/10.1016/S1365-1609\(99\)00093-3](https://doi.org/10.1016/S1365-1609(99)00093-3)
- Zbinden, D., Rinaldi, A. P., Urpi, L., & Wiemer, S. (2017). On the physics-based processes behind production-induced seismicity in natural gas fields. *Journal of Geophysical Research: Solid Earth*, 122, 3792–3812. <https://doi.org/10.1002/2017JB014003>
- Zhang, J., Wong, T., & Davis, D. M. (1990). Micromechanics of pressure-induced grain crushing in porous rocks, 95, 341–352.
- Zoback, M. D. (2007). *Reservoir Geomechanics*. Cambridge, UK: Cambridge University Press.